CrystEngComm

PAPER

View Article Online
View Journal | View Issue

Open Access Article. Published on 17 April 2023. Downloaded on 8/9/2025 3:58:16 PM.
This article is licensed under a Creative Commons Attribution 3.0 Unported Licence.

Check for updates

Cite this: *CrystEngComm*, 2023, **25**, 2739

Pyridine-driven assembly of Zn(II) and Cd(II) complexes with 2-furoic acid. The role of water in a structural transformation†

Daniel Ejarque,[a] Francisco Sánchez-Férez,[a] Núria Félez-Guerrero,[a] Teresa Calvet,[b] Mercè Font-Bardia[c] and Josefina Pons *[a]

Understanding the factors governing the self-assembly of organic ligands with metal ions is essential to engineering target molecular arrangements with the desired properties. Indeed, small modifications of the synthetic conditions lead to the obtention of different complexes, varying from discrete monomers to coordination polymers (CPs). Based on the potential coordinating ability of 2-furoic acid (2-FA), we prepared five Zn(II) and Cd(II) complexes to study the behavior of the furane O atom and the competitiveness of the M–O bond formation in methanol (MeOH). Reactions between $M(OAc)_2{\cdot}2H_2O$ (M = Zn(II), Cd(II)), 2-FA, and two *p*-substituted pyridine ligands (isonicotinamide (Isn) and 4-acetylpyridine (4-Acpy)) in MeOH yielded the two dimers $[Zn(\mu\text{-}2\text{-FA})(2\text{-FA})(Isn)_2]_2$ (**1**) and $[Cd(\mu\text{-}2\text{-FA})(2\text{-FA})(Isn)_2]_2$ (**2**), the dimeric paddle-wheel $[Zn(\mu\text{-}2\text{-FA})_2(4\text{-Acpy})]_2$ (**3**), and the monomer $[Cd(2\text{-FA})_2(4\text{-Acpy})_2(OH_2)]$ (**4**). Their crystal structures have been studied, observing diverse coordination numbers between five and seven and diverse coordination modes of the carboxylate groups. Interestingly, the recrystallization of **4** in acetonitrile (ACN) resulted in a dissolution–recrystallization structural transformation (DRST), leading to an intricate coordination polymer (CP) with the formula $\{[Cd(\mu\text{-}2\text{-FA})(2\text{-FA})(OH_2)_2]_n[Cd(\mu\text{-}2\text{-FA})(2\text{-FA})(4\text{-Acpy})(OH_2)]_n\}$ (**5**) exhibiting coordination of the furane O atom. Within this collection of arrangements, 2-FA displayed a great diversity of coordination modes that were combined and interchanged in the DRST process. Their photophysical properties in solution have been analyzed and their quantum yields calculated. Likewise, further insight into the DRST process was obtained from fluorescence measurements. From these results, a pathway for the structural transformation highlighting the crucial role of solvents has been proposed.

Received 3rd February 2023,
Accepted 19th March 2023

DOI: 10.1039/d3ce00104k

rsc.li/crystengcomm

Introduction

The rational design of d^{10} coordination complexes has emerged as an outstanding research area benefitting from their application in the field of optical materials as luminophores,[1,2] their importance in sensing devices,[3] or their photoelectrical conductivity.[4,5] The soft nature of Zn(II) and Cd(II) ions enables a great structural diversity and coordination versatility, giving access to a plethora of arrangements guided only by the ligands' steric requirements and the size of the d^{10} metal ion. Hence, accessible coordination numbers of d^{10} carboxylates range from four to six for Zn(II), while Cd(II) tends to form coordination numbers up to seven. Zn(II) carboxylates display an almost equal tendency to form either the paddle-wheel or the dimeric arrangement assembled by four or two bridging (μ_2:η^1:η^1) carboxylate moieties, forming the $[Zn_2(CO_2)_4]$ or $[Zn_2(CO_2)_2]$ secondary building units (SBUs), respectively. Instead, Cd(II) carboxylates display the dimeric array $[Cd_2(CO_2)_2]$ as the most common arrangement subsequently followed by the dimeric array with two additional chelate (μ_1:η^2) ligands denoted as $[Cd_2(CO_2)_4]$-2 + 2. After the introduction of pyridine derivatives, the preferred arrangements are barely altered, only leading to a further increase in dimensionality.[6]

Regarding the structure of discrete molecular Zn(II) and Cd(II) carboxylate complexes with N-donor ligands, a search in the CSD[7] has revealed that the Zn(II) tendency is shifted towards the formation of the dimeric paddle-wheel (112 hits) with respect to the dimer (4 hits).[8–11] However, Cd(II) preferentially accommodates the $[Cd_2(CO_2)_4]$-2 + 2 dimeric array (82 hits). Interestingly, the combination of d^{10} metal

[a] Departament de Química, Universitat Autònoma de Barcelona, 08193-Bellaterra, Barcelona, Spain. E-mail: josefina.pons@uab.es
[b] Departament de Mineralogia, Petrologia i Geologia Aplicada, Universitat de Barcelona, Martí i Franquès s/n, 08028 Barcelona, Spain
[c] Unitat de Difracció de Raig-X, Centres Científics i Tecnològics de la Universitat de Barcelona (CCiTUB), Universitat de Barcelona, Solé i Sabarís, 1-3, 08028 Barcelona, Spain

† Electronic supplementary information (ESI) available. CCDC 2239452–2239456. For ESI and crystallographic data in CIF or other electronic format see DOI: https://doi.org/10.1039/d3ce00104k

Open Access Article. Published on 17 April 2023. Downloaded on 8/9/2025 3:58:16 PM.
This article is licensed under a Creative Commons Attribution 3.0 Unported Licence.

carboxylates and pyridine derivatives has already led to the formation of excellent luminophores.[12]

Our group has previously studied the coordination chemistry of d^{10} metal ions towards carboxylic acids holding ether groups,[13,14] observing that Hg(II) and Hg(I) have a preferential interaction over Zn(II) and Cd(II) with these O atoms, leading to the arrangement of unusual structures. Instead, in the presence of Zn(II) and Cd(II), the dioxole O atoms did not participate in the coordination environment and only promoted weak C–H···O interactions.[13] Continuing with this research, we selected 2-furoic acid (2-FA) and two pyridine derivatives (dPy), namely, isonicotinamide (Isn) and 4-acetylpyridine (4-Acpy), to further study the crystal engineering of Zn(II) and Cd(II) carboxylates with N-donor ligands in the presence of ether O atoms. There are a few reported cases in which the ether O atom of furane carboxylic acid partakes in the coordination towards Zn(II) and Cd(II), but in those examples, the formation of the M–O bond is supported by a bridging bis-chelate (μ_2:η^2:η^1:η^1) coordination mode (Fig. 1).[15–17] This double-chelate arrangement together with the formation of two five-membered rings is probably driving the coordination of the furane O atom.

Although the 2-FA ligand can only be found coordinated by the furane O atom in a heterometallic Zn(II)/Na arrangement,[18] we envisioned that it could promote the coordination of the furane O atom to the metal center supported by the formation of one five-membered ring that provides better stabilization to bigger ions, and thus it will preferentially support Cd–O bond formation over the Zn(II) ion. Nevertheless, when dealing with ligands bearing weak coordinating atoms able to act as hemilabile linkers,[19] competitive bond formation with additional solvent molecules can occur.[20,21] From these data, it is also inferred that strong intra- and intermolecular interactions can displace the coordination of additional carboxylate O atoms, guiding a lower denticity and shifting from chelate to bridged or even to monodentate.[22–26] Within this frame, structural transformations arose as a fundamental process guiding the arrangement of molecular and extended entities.[27,28] Among them, those occurring in the solid state are denoted as solid-state structural transformations (SSSTs), in which the switching between single crystal to single crystal (SCSC) is predominant.[29,30] In this regard, SCSC transformations demonstrated promising applications as molecular switches[31] or in molecular capture.[32] Conversely, the transformations involving the dissolution, bond breaking, and rearrangement into a different array are referred to as dissolution–recrystallization structural transformations (DRSTs).[33,34] Despite the ongoing research in this field, there is still the need for a better understanding of the factors governing this process as well as to provide further mechanistic insights.[35,36] Interestingly, DRST processes have shown promising results, presenting changes in their magnetic[35,37] or photophysical properties.[28,36] Aiming at the furane O coordination, we selected the $[M_2(CO_2)_4]$-2 + 2 dimeric array as the model structure from the available accessible arrangements. We surmised that the higher distortion in these dimers could enable decoordination, inducing available coordination sites in the metal center that can be filled by weaker coordinating atoms. Hence, the choice of Isn was based on the guided arrangement into dimeric Zn(II) complexes driven by the amide–amide homosynthon,[11] otherwise obtaining the dimeric paddle-wheel, whereas 4-Acpy was selected as a non-guiding ligand for better comparison.[38] Therefore, we conducted the reaction of Zn(II) and Cd(II) with 2-FA and Isn or 4-Acpy. From these reactions, we have isolated five complexes bearing two isostructural dimeric $[Zn(\mu\text{-2-FA})(2\text{-FA})(Isn)_2]_2$ (**1**) and $[Cd(\mu\text{-2-FA})(2\text{-FA})(Isn)]_2]_2$ (**2**) arrays, a dimeric paddle-wheel ($[Zn(\mu\text{-2-FA})_2(4\text{-Acpy})]_2$ (**3**), a monomeric $[Cd(2\text{-FA})_2(4\text{-Acpy})_2(OH_2)]$ (**4**), and a polymeric structure $\{[Cd(\mu\text{-2-FA})_2(OH_2)_2]_n[Cd(\mu\text{-2-FA})_2(4\text{-Acpy})(OH_2)]_n\}$ (**5**) (Scheme 1).

Within this series, the 2-FA ligand presented the whole range of coordination modes from μ_1:η^1 to μ_1:η^2:η^1. Interestingly, complex **5** has been obtained from a DRST process[21,39] starting from **4** and presented an unusual μ_2:η^2:η^1:η^1-coordination mode which is, to the best of our knowledge, the first reported case in which the furane O atom of 2-FA participates in the coordination towards the Cd(II) ion. Furthermore, the photophysical properties in solution of the aforementioned complexes have been compared to those of the previously reported analogues.[11] In addition, the structural transformation is found to be accompanied by a significant change in emission, and thus fluorescence experiments were used to trace the conversion of **4** to **5**, ensuring the importance of both solvent and water molecules in the transformation. From these results, a pathway for the DRST process from **4** to **5** has been proposed.

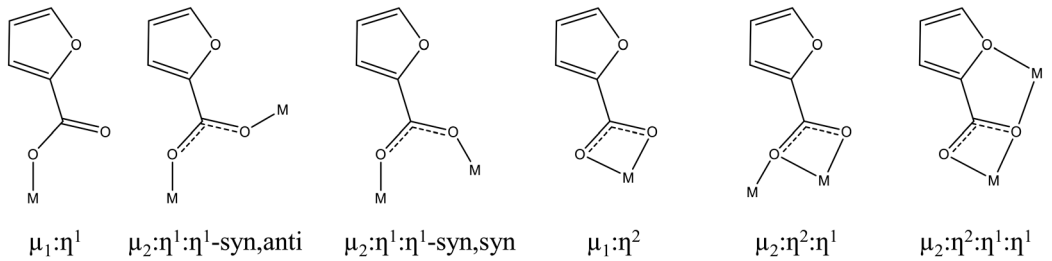

Fig. 1 Potential coordination modes of 2-FA ligand in Zn(II) and Cd(II) complexes.

Open Access Article. Published on 17 April 2023. Downloaded on 8/9/2025 3:58:16 PM.
This article is licensed under a Creative Commons Attribution 3.0 Unported Licence.

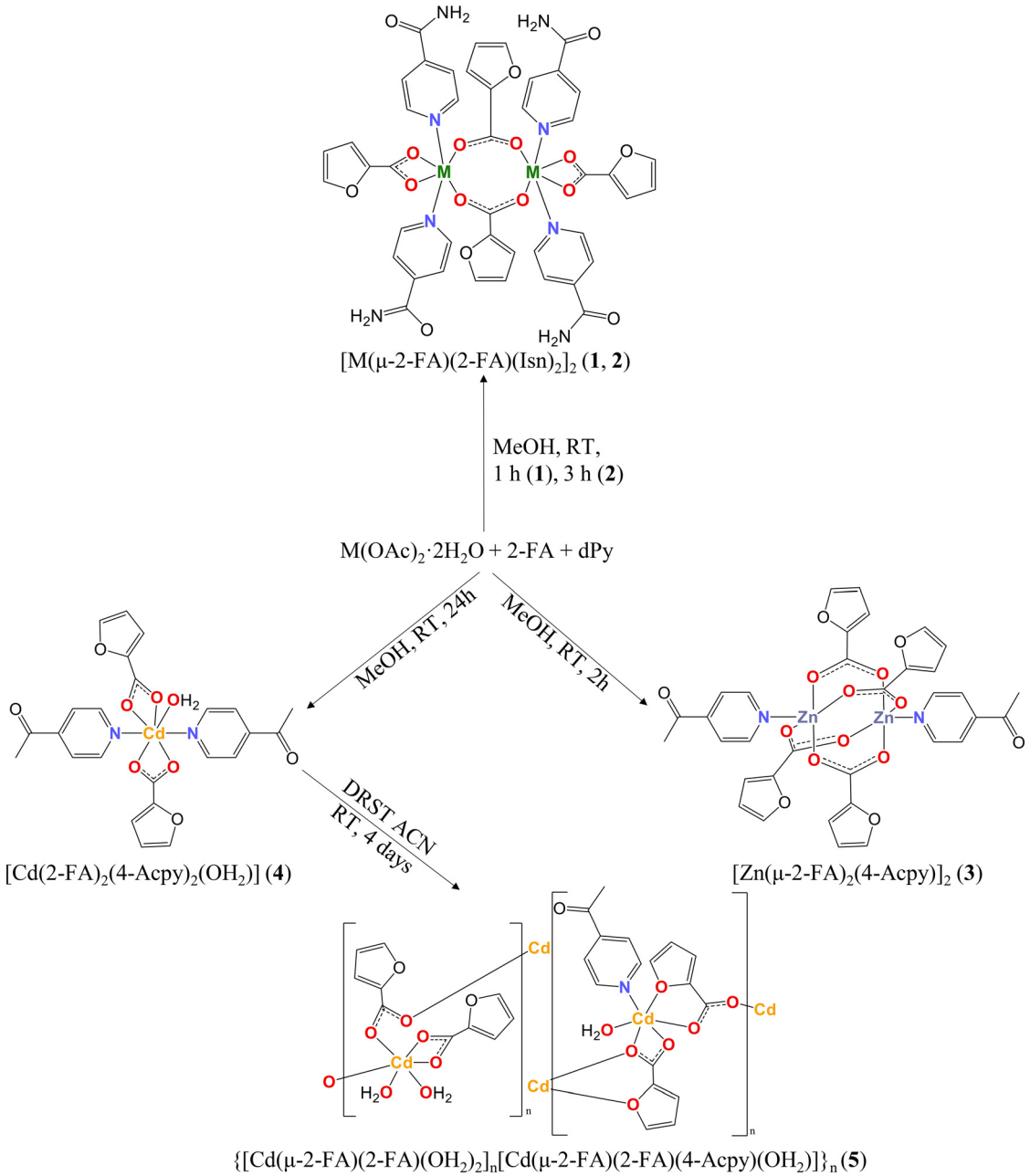

Scheme 1 Outline of the preparation of complexes **1**–**4** and DRST from **4** to **5**.

Experimental section

Materials and general methods

Zinc(II) acetate dihydrate ($Zn(OAc)_2{\cdot}2H_2O$), cadmium(II) acetate dihydrate ($Cd(OAc)_2{\cdot}2H_2O$), 2-furoic acid (2-FA), isonicotinamide (Isn), and 4-acetylpyridine (4-Acpy) ligands, acetonitrile (ACN) (≥99.5%), diethyl ether (Et_2O), *n*-heptane, and methanol (MeOH) (99.5%) as solvents were purchased from Sigma-Aldrich. Deuterated dimethyl sulfoxide (DMSO-d_6) was purchased from Eurisotop. All of them were used without further purification. All the reactions and manipulations were carried out in air at room temperature (RT). Powder X-ray diffraction (PXRD) patterns were recorded from a 2θ angle of 5° to 30° and a step scan of 0.01671°, using a Panalytical X'pert PRO MPD apparatus with a monochromatic CuKα radiation with λ = 1.5406 Å. Elemental analyses (C, H, N) were carried out on a Thermo Scientific Flash 2000 CHNS Analyzer. FTIR-ATR spectra were recorded on a Perkin Elmer spectrometer equipped with an attenuated total reflectance (ATR) accessory (model MKII Golden Gate) with a diamond window in the range 4000–500 cm^{-1}. ^1H and $^{13}C\{^1H\}$ NMR spectra of **1**–**5** as well as DEPT-135 NMR spectra of **2** were recorded on a Bruker Ascend 300 MHz spectrometer in DMSO-d_6 solutions at RT. All the chemical shifts (δ) are given in ppm relative to Me_4Si as an internal standard. Thermogravimetric analysis (TGA) was conducted

Open Access Article. Published on 17 April 2023. Downloaded on 8/9/2025 3:58:16 PM.
This article is licensed under a Creative Commons Attribution 3.0 Unported Licence.

using 2.204 mg (**1**), 3.147 mg (**2**), 2.835 mg (**3**), 2.255 mg (**4**), and 3.818 mg (**5**) in a TGA 7 Perkin Elmer thermobalance, using an open platinum crucible. The heating ramp was set to 5 °C min^{-1} from 50 to 330 °C under a nitrogen flow rate of 60 mL min^{-1}. The electronic spectra in MeOH (anhydrous, 99.8%, Sigma-Aldrich) solution for **1**–**4**, in ACN (HPLC grade, Sigma-Aldrich) solution for **5**; and in Milli-Q water for L-tyrosine (L-tyr) were run on an Agilent HP 8453 UV-vis spectrophotometer with a quartz cell having a path length of 1 cm in the range of 190–500 nm. Fluorescence measurements were carried out with a Perkin Elmer LS 55 50 Hz Fluorescence Spectrometer using a 1 cm quartz cell in MeOH (anhydrous, 99.8%, Sigma-Aldrich) (**1**–**4**), ACN (HPLC grade, Sigma-Aldrich) (**5**), and Milli-Q water (L-tyr) solutions. In addition, the fluorescence measurements to trace the DRST from **4** to **5** were done using ACN (≥99.5%). All the emission spectra were measured at 25 °C. The samples were excited at their maximum emission wavelength and their emission was recorded between 200 and 600 nm. The data obtained were corrected by means of the Origin Pro 2019b software. A CIE 1931 chromaticity diagram was generated using Origin Pro 2019b software.

Preparation of compounds 1 and 2

A MeOH solution (1 mL) of 2-FA (102 mg, 0.910 mmol (**1**); 87.0 mg, 0.776 mmol (**2**)) was added dropwise to a MeOH solution (1 mL) of $M(OAc)_2{\cdot}2H_2O$ (100 mg, 0.456 mmol, M = Zn(II) (**1**); 103 mg, 0.386 mmol, M = Cd(II) (**2**)) at RT under constant stirring. Then, a MeOH solution (1.5 mL) of Isn (231 mg, 1.89 mmol (**1**); 95.0 mg, 0.778 mmol (**2**)) was added dropwise to the mixture at RT, observing immediately the formation of a white precipitate, and was left stirring for 1 h (**1**) or 3 h (**2**). The powder was filtered, washed twice with 10 mL of cold Et_2O, and dried under vacuum. Single crystals suitable for X-ray diffraction were obtained by recrystallization in MeOH after one week (**1**) or one day (**2**) at RT.

(**1**) Yield: 204 mg (84.2% with respect to $Zn(OAc)_2{\cdot}2H_2O$). Elem. anal. calc. for $C_{44}H_{36}Zn_2N_8O_{16}$ (1063.58): C 49.69; H 3.41; N 10.54; found: C, 49.48; H 3.24; N 10.31. FTIR-ATR (wavenumber, cm^{-1}): 3312(w) [ν(N–H)], 3161(w) [ν(N–H)], 3069(w) [ν(C–H)]$_{ar}$, 1699(m) [ν(C═O)], 1609(s), 1555(s) [ν_{as}(COO)], 1481(s) [ν(C═C/C═N)], 1420(s) [ν_s(COO)], 1397(s) [ν_s(COO)], 1372(s) [δ(C═C/C═N)], 1227(m), 1196(m) [ν(C–O–C)], 1148(m), 1121(w) [ν(C–O–C)], 1099(w), 1080(w), 1067(w), 1018(m) [δ_{ip}(C–H)], 1009(m), 935(w), 885(m), 860(w), 823(m), 783(s) [δ_{oop}(C–H)], 750(s) [δ_{oop}(C–H)], 679(w), 642(s), 615(s), 594(m), 519(w), 505(w). ^{1}H NMR (300 MHz; DMSO-d_6, Me_4Si, 298 K): δ = 8.76 [2H, m, *o*–H], 8.25 [1H, m, OC–NH_{syn}], 7.76 [4H, m, m–H + OC–NH_{anti} + O–CH–CH–CH], 6.93 [1H, m, O–CH–CH–CH], 6.55 [1H, m, O–CH–CH–CH]. $^{13}C\{^1H\}$ NMR (75 MHz, DMSO-d_6, Me_4Si, 298 K): δ = 166.5 [H_2N–CO], 163.8 [O_2C], 150.3 [N–CH], 149.1 [O_2C–C], 144.9 [O–CH–CH–CH], 141.8 [N–CH–CH–C], 122.0 [N–CH–CH], 115.0 [O–CH–CH–CH], 111.6 [O–CH–CH–CH].

(**2**) Yield: 132 mg (60.8% with respect to $Cd(OAc)_2{\cdot}2H_2O$). Elem. anal. calc. for $C_{44}H_{36}Cd_2N_8O_{16}$ (1157.61): C 45.65; H 3.13; N 9.68. Found: C, 45.54; H 3.09; N 9.49. FTIR-ATR (wavenumber, cm^{-1}): 3299(w) [ν(N–H)], 3172(w) [ν(N–H)], 3144–3066 (br) [ν(C–H)]$_{ar}$, 1696(m) [ν(C═O)], 1612(w), 1588(m), 1557(s) [ν_{as}(COO)], 1480(s) [ν(C═C/C═N)], 1411(sh) [ν_s(COO)], 1399(s) [ν_s(COO)], 1368(s) [δ(C═C/C═N)], 1226 (m), 1195(m) [ν(C–O–C)], 1147(m), 1119(w) [ν(C–O–C)], 1098(w), 1080(w), 1067(w), 1017(m) [δ_{ip}(C–H)], 933(w), 885(w), 859(w), 820(m), 783(m) [δ_{oop}(C–H)], 752(m) [δ_{oop}(C–H)], 677(w), 644(m), 612(m), 599 (m), 527(m), 513(w). ^{1}H NMR (300 MHz, DMSO-d_6, Me_4Si, 298 K): δ = 8.71 [2H, dd^3, J = 4.4 Hz; ^4J = 1.7 Hz, o–H], 8.23 [1H, m, OC–NH_{syn}], 7.76 [2H, dd, ^3J = 4.4 Hz; ^4J = 1.7 Hz, *m*–H], 7.69 [2H, m, OC–NH_{anti} + O–CH–CH–CH], 6.87 [1H, m, O–CH–CH–CH], 6.51 [1H, m, O–CH–CH–CH]. $^{13}C\{^1H\}$ NMR (75 MHz, DMSO-d_6; Me_4Si; 298 K): δ = 166.3 [H_2N–CO], 164.5 [O_2C], 150.3 [N–CH], 149.7 [O_2C–C], 144.5 [O–CH–CH–CH], 141.6 [N–CH–CH–C], 121.6 [N–CH–CH], 114.5 [O–CH–CH–CH], 111.4 [O–CH–CH–CH]. DEPT-135 NMR (75 MHz, DMSO-d_6; Me_4Si; 298 K): δ = 150.3 [N–CH], 144.5 [O–CH–CH–CH], 121.7 [N–CH–CH], 114.5 [O–CH–CH–CH], 111.4 [O–CH–CH–CH].

Preparation of compounds 3 and 4

To a MeOH solution (1 mL) of $M(OAc)_2{\cdot}2H_2O$ (100 mg, 0.456 mmol, M = Zn(II) (**3**); 102 mg, 0.383 mmol, M = Cd(II) (**4**)), 4-Acpy (0.208 mL, 1.87 mmol (**3**); 0.087 mL, 0.783 mmol (**4**)) was added dropwise at RT under constant stirring. Afterward, a MeOH solution (1 mL) of 2-FA (105 mg, 0.918 mmol (**3**); 87.0 mg, 0.776 mmol (**4**)) was added to the mixture. The reaction was left stirring for 2 h (**3**) and 24 h (**4**) at RT and then, a white solid precipitated for **3**, while the reaction mixture of **4** was concentrated under vacuum and kept in the fridge for 3 days until a white solid was obtained. The resulting solids were filtered, washed twice with 10 mL of cold Et_2O and dried under vacuum. Single crystals suitable for X-ray diffraction were obtained by recrystallization in MeOH (**3**) or MeOH/EtOH (**4**) after keeping the solution in the fridge for three weeks (**3**) or letting it evaporate at RT for four days (**4**).

(**3**) Yield: 74.0 mg (39.7% with respect to $Zn(OAc)_2{\cdot}2H_2O$). Elem. anal. calc. for $C_{34}H_{26}Zn_2N_2O_{14}$ (817.35): C 49.96; H 3.21; N 3.43. Found: C, 49.69; H 3.15; N 3.21. FTIR-ATR (wavenumber, cm^{-1}): 3150–3105(br) [ν(C–H)]$_{ar}$, 1701(m) [ν(C═O)], 1640(s) [ν(C═C/C═N)], 1591(m), 1574(m) [ν_{as}(COO)], 1479(s), 1415(s) [ν_s(COO)], 1367(s) [δ(C═C/C═N)], 1326(m), 1268(m), 1229(m), 1196(m) [ν(C–O–C)], 1142(m), 1076(m), 1063(m), 1012(m) [δ_{ip}(C–H)], 962(m), 882(m), 827(m), 798(m), 781(s) [δ_{oop}(C–H)], 755(s) [δ_{oop}(C–H)], 663(m), 616(m), 595(m). ^{1}H NMR (300 MHz, DMSO-d_6, 298 K): 8.83 [2H, d, ^3J = 3.8 Hz, o–H], 7.85 [2H, dd, ^3J = 6.0 Hz; ^4J = 1.2 Hz, m–H], 7.72 [2H, dd, ^3J = 1.5 Hz; ^4J = 0.7, O–CH–CH–CH], 6.93 [2H, dd, ^3J = 3.3 Hz; ^4J = 0.5 Hz, O–CH–CH–CH], 6.52 [2H, dd, ^3J = 3.3 Hz; ^4J = 1.7 Hz, O–CH–CH–CH], 2.63 [3H, s, CH_3]. $^{13}C\{^1H\}$ NMR (75 MHz, DMSO-d_6, 298 K): 198.1 [H_3C–CO],

Open Access Article. Published on 17 April 2023. Downloaded on 8/9/2025 3:58:16 PM.
This article is licensed under a Creative Commons Attribution 3.0 Unported Licence.

163.7 [O_2C], 150.8 [N–CH], 149.1 [O_2C–C], 144.7 [O–CH–CH–CH], 143.0 [N–CH–CH–C], 121.7 [N–CH–CH], 114.8 [O–CH–CH–CH], 111.5 [O–CH–CH–CH], 27.0 [CH_3].

(**4**) Yield: 132 mg (58.0% with respect to $Cd(OAc)_2{\cdot}2H_2O$). Elem. anal. calc. for $C_{24}H_{22}CdN_2O_9$ (594.85): C 48.46; H 3.73; N 4.71. Found: C, 48.69; H 3.55; N 4.41. FTIR-ATR (wavenumber, cm^{-1}): 3202–3066(br) [ν(O–H)], 3051(w) [ν(C–H)]$_{ar}$, 2997–2920(br) [ν(C–H)]$_{al}$, 1698(w) [ν(C═O)], 1684(m) [ν(C═O)], 1589(m), 1540(s) [ν_{as}(COO)], 1481(m) [ν(C═C/C═N)], 1413(s) [ν_s(COO)], 1362(s) [δ(C═C/C═N)], 1260(m), 1224(m), 1193(m) [ν(C–O–C)], 1011 (m) [δ_{ip}(C–H)], 816(s) [δ_{oop}(C–H)], 783(m), 736(m), 591(s). ^{1}H NMR (300 MHz, DMSO-d_6, 298 K): 8.81 [4H, d, ^3J = 5.8 Hz, o–H], 7.82 [4H, d, ^3J = 4.8 Hz, m–H], 7.70 [2H, d, ^3J = 0.7 Hz, O–CH–CH–CH], 6.90 [2H, dd, ^3J = 3.3 Hz; ^4J = 1.7 Hz, O–CH–CH–CH], 6.51 [2H, dd, ^3J = 3.3 Hz; ^4J = 1.7 Hz, O–CH–CH–CH], 2.62 [6H, s, CH_3]. $^{13}C\{^1H\}$ NMR (75 MHz, DMSO-d_6, 298 K): 198.1 [H_3C–CO], 164.6 [O_2C], 150.8 [N–CH], 149.7 [O_2C–C], 144.5 [O–CH–CH–CH], 142.9 [N–CH–CH–C], 121.6 [N–CH–CH], 114.5 [O–CH–CH–CH], 111.4 [O–CH–CH–CH], 26.9 [CH_3].

DRST of compound 5

Complex **4** (22.2 mg, 0.037 mmol) was dissolved in 4 mL of ACN (≥99.5%) and was left to slowly evaporate at RT until colorless prismatic crystals were formed after four days. The resulting crystals were washed twice with 10 mL of *n*-heptane and dried under vacuum.

Yield: 13.8 mg (87.6% with respect to **4**). Elem. anal. calc. for $C_{27}H_{25}Cd_2NO_{16}$ (844.31): C, 38.41; H, 2.98; N, 1.66. Found: C, 38.29; H, 2.74; N, 1.39. FTIR-ATR (wavenumber, cm^{-1}): 3488–3250(br) [ν(O–H)], 3144(w) [ν(C–H)$_{ar}$], 1697(m) [ν(C═O)], 1591(m), 1543(s) [ν_{as}(COO)], 1477(s) [ν(C═C/C═N)], 1411(s) [ν_s(COO)], 1399(s) [ν_s(COO)], 1365 (s) [δ(C═C/C═N)], 1330(m), 1273(m), 1229(m), 1221(m), 1193(m) [ν(C–O–C)], 1140(w), 1074(w), 1065(w), 1017(m) [δ_{ip}(C–H)], 968(w), 932(w), 884(w), 859(w), 826(m), 815(m) [δ_{oop}(C–H)], 781(s) [δ_{oop}(C–H)], 756(s) [δ_{oop}(C–H)], 666(m), 616(m), 593(s), 529(m), 501(s). ^{1}H NMR (300 MHz, DMSO-d_6, 298 K): 8.81 [2H, dd, ^3J = 4.4 Hz, ^4J = 1.6 Hz, o–H], 7.81 [2H, dd, ^3J = 4.4 Hz, ^4J = 1.7 Hz, m–H], 7.70 [4H, dd, ^3J = 1.7 Hz, ^3J = 0.8 Hz, O–CH–CH–CH], 6.89 [4H, dd, ^3J = 3.3 Hz; ^4J = 0.8 Hz, O–CH–CH–CH], 6.51 [4H, dd, ^3J = 3.3 Hz; ^4J = 1.8 Hz, O–CH–CH–CH], 2.62 [3H, s, CH_3]. $^{13}C\{^1H\}$ NMR (75 MHz, DMSO-d_6, 298 K): 198.2 [H_3C–CO], 164.4 [O_2C], 150.9 [N–CH], 149.7 [O_2C–C], 144.4 [O–CH–CH–CH], 142.6 [N–CH–CH–C], 121.4 [N–CH–CH], 114.4 [O–CH–CH–CH], 111.4 [O–CH–CH–CH], 26.9 [CH_3].

X-ray crystallographic data

Colorless (**1**–**5**) specimens were used for the X-ray crystallographic analysis (Tables 1 and 2).

The X-ray intensity data were measured on a D8 Venture system equipped with a multilayer monochromator and a Mo microfocus (λ = 0.71073 Å). For all the compounds, the frames were integrated using the Bruker SAINT software package using a narrow-frame algorithm. The structures were solved and refined using a SHELXTL Software Package (version-2018/3).[40] The integration of the data with a 0.80 Å (**1** and **2**) and 0.70 Å (**3**–**5**) resolution, of which 4693 (**1**), 4759 (**2**), 10 156 (**3**), 7294 (**4**), and 9453 (**5**) reflections were independent, gave an average redundancy of 11.443 (**1**), 1.000 (**2**), 14.699 (**3**), 9.126 (**4**), and 3.927 (**5**), completeness of 99.9% (**1**), 99.7% (**2**), 99.9% (**3**), 99.6% (**4**), and 99.0% (**5**), R_{sig} of 5.88% (**1**), 10.56% (**2**), 1.78% (**3**), 6.63% (**4**), and 2.80% (**5**), presenting 3681 (78.44%) (**1**), 2688 (56.48%) (**2**), 9552 (94.05%) (**3**), 5785 (79.31%) (**4**), and 9106 (96.33%) (**5**) reflections greater than $2\sigma(|F|^2)$.

For **1**–**5** the final cell constants and volume are based upon refinement of the XYZ centroids of reflections above 20 $\sigma(I)$. Data were corrected for absorption effects using the multi-scan method (SADABS). Crystal data and additional details of structure refinement for **1**–**5** are reported in

Table 1 Crystal data and structure refinement for **1** and **2**

	1	**2**
Empirical formula	$C_{44}H_{36}Zn_2N_8O_{16}$	$C_{44}H_{36}Cd_2N_8O_{16}$
Formula weight	1063.55	1157.61
T (K)	100(2)	100(2)
Wavelength (Å)	0.71073	0.71073
System, space group	Monoclinic, $P2_1/c$	Monoclinic, $P2_1/c$
Unit cell dimensions		
a (Å)	11.0553(7)	11.1356(18)
b (Å)	13.6054(10)	13.457(2)
c (Å)	15.7426(10)	15.870(2)
α (°)	90	90
β (°)	104.307	103.005(4)
γ (°)	90	90
V (Å^3)	2294.4(3)	2317.2(7)
Z	2	2
D_{calc} (mg m^{-3})	1.539	1.659
μ (mm^{-1})	1.127	0.998
F (000)	1088	1160
Crystal size (mm^3)	0.135 × 0.031 × 0.016	0.155 × 0.027 × 0.023
hkl ranges	$-13 \le h \le 13$ $-17 \le k \le 17$ $-19 \le l \le 19$	$-13 \le h \le 13$ $0 \le k \le 16$ $0 \le l \le 19$
θ range (°)	1.901 to 26.404	1.877 to 26.463
Reflections collected/unique/[R_{int}]	53 701/4693/0.1346	4759/4759/0.2442
Completeness to θ (%)	100.0	100.0
Absorption correction	Semi-empirical from equivalents	Semi-empirical from equivalents
Max. and min. transmission	0.7454 and 0.6222	0.7454 and 0.4775
Refinement method	Full-matrix least-squares on $\|F\|^2$	Full-matrix least-squares on $\|F\|^2$
Data/restraints/parameters	4693/0/286	4759/4/286
Goodness of fit on F^2	1.088	0.968
Final R indices [$I > 2\sigma(I)$]	R_1 = 0.0628, wR_2 = 0.1158	R_1 = 0.0360, wR_2 = 0.0662
R indices (all data)	R_1 = 0.0863, wR_2 = 0.1243	R_1 = 0.1056, wR_2 = 0.0936
Absolute structure parameter	n/a	n/a
Extinction coefficient	n/a	n/a
Largest diff. peak and hole (e Å^{-3})	0.443 and −0.980	1.595 and −0.747

Open Access Article. Published on 17 April 2023. Downloaded on 8/9/2025 3:58:16 PM.
This article is licensed under a Creative Commons Attribution 3.0 Unported Licence.

Table 2 Crystal data and structure refinement for 3–5

	3	4	5
Empirical formula	$C_{34}H_{26}Zn_2N_2O_{14}$	$C_{24}H_{22}CdN_2O_9$	$C_{27}H_{25}Cd_2NO_{16}$
Formula weight	817.31	594.83	844.28
T (K)	100(2)	100(2)	100(2)
Wavelength (Å)	0.71073	0.71073	0.71073
System, space group	Tetragonal, $P4_3$	Triclinic, $P\bar{1}$	Monoclinic, $P2_1$
Unit cell dimensions			
a (Å)	11.7905(4)	9.2175(3)	12.3981(6)
b (Å)	11.7905(4)	11.0467(5)	8.4459(3)
c (Å)	23.9682(8)	13.4532(6)	15.1806(7)
α (°)	90	104.477(2)	90
β (°)	90	101.662(2)	104.276(2)
γ (°)	90	109.6270(10)	90
V (Å^3)	3332.0(3)	1186.22(9)	1540.52(12)
Z	4	2	2
D_{calc} (mg m^{-3})	1.629	1.665	1.820
μ (mm^{-1})	1.515	0.978	1.457
F (000)	1664	600	836
Crystal size (mm^3)	0.276 × 0.153 × 0.069	0.061 × 0.025 × 0.012	0.132 × 0.087 × 0.040
hkl ranges	$-16 \le h \le 16$	$-13 <= h <= 13$	$-17 \le h \le 17$
	$-16 \le k \le 16$	$-15 <= k <= 15$	$-12 \le k \le 12$
	$-34 \le l \le 34$	$-19 <= l <= 19$	$-21 \le l \le 21$
θ range (°)	1.925 to 30.517	2.085 to 30.621	2.439 to 30.732
Reflections collected/unique/[R_{int}]	149 278/10 156/0.0442	66 566/7294/0.1313	37 126/9453/0.0299
Completeness to θ (%)	99.9	100.0	99.8
Absorption correction	Semi-empirical from equivalents	Semi-empirical from equivalents	Semi-empirical from equivalents
Max. and min. transmission	0.7444 and 0.6605	0.7461 and 0.5736	0.7461 and 0.6472
Refinement method	Full-matrix least-squares on $\|F\|^2$	Full-matrix least-squares on $\|F\|^2$	Full-matrix least-squares on $\|F\|^2$
Data/restraints/parameters	10 156/4/472	7294/3/333	9453/10/402
Goodness of fit on F^2	1.033	1.049	1.037
Final R indices [$I > 2\sigma(I)$]	R_1 = 0.0298,	R_1 = 0.0448,	R_1 = 0.0272,
	wR_2 = 0.0809	wR_2 = 0.0920	wR_2 = 0.0645
R indices (all data)	R_1 = 0.0335,	R_1 = 0.0693,	R_1 = 0.0292,
	wR_2 = 0.0835	wR_2 = 0.1033	wR_2 = 0.0658
Absolute structure parameter	n/a	n/a	0.18(2)
Extinction coefficient	n/a	n/a	n/a
Largest diff-peak and hole (e Å^{-3})	0.611 and −0.434	1.535 and −1.058	2.254 and −1.073

Tables 1 and 2. Complete information about the crystal structure and molecular geometry is available in CIF format *via* CCDC 2239454 (**1**), 2239452 (**2**), 2239456 (**3**), 2239453 (**4**), and 2239455 (**5**). Molecular graphics were generated using Mercury 4.3.1 software,[41] using the POV-Ray image package.[42] The color codes for all the molecular graphics are as follows: dark blue (Zn), light orange (Cd), red (O), light blue (N), gray (C), and white (H). The evaluation of the geometry distortion of the metal cores in **1–5** was carried out using version 2.1 of SHAPE software from the corresponding .cif files.[43] Further discussion of the extended structures of **1–5** is provided in the ESI.†

Results and discussion

Preparation of 1–5

Complexes **1–4** were obtained by reaction of $M(OAc)_2{\cdot}2H_2O$ (M = Zn(II), Cd(II)) and 2-FA with their corresponding dPy ligands (Isn, **1** and **2**; 4-Acpy, **3** and **4**) in MeOH at room temperature (RT). Compounds **1** and **3** were prepared using a 1 : 2 : 4 molar ratio, while **2** and **4** were synthesized with a 1 : 2 : 2 molar ratio. The corresponding single crystals suitable for X-ray crystallographic analysis were grown *via* recrystallization in MeOH (**1** and **3**) or MeOH/EtOH (**4**) and by slow evaporation of the mother liquors (**2**). In addition, the recrystallization of **4** in ACN (≥99.5%) resulted in the DRST process yielding the coordination polymer **5**. The selection of ACN was done aiming to minimize hydrogen bond interactions that can abstract and compete with the coordination of the weakly coordinating O atom from the furane ring.[22,24–26]

General characterization

Compounds **1–5** were characterized by powder X-ray diffraction (PXRD), elemental analysis (EA), FTIR-ATR, ^{1}H, ^{13}C{^{1}H} NMR spectroscopy, thermogravimetric analysis (TGA), and single-crystal X-ray diffraction method. The phase purity of the samples was confirmed by PXRD. The corresponding patterns can be found in the ESI,† Fig. S1–S5. The EA of all the compounds agrees with the proposed formulas. TGA of complexes **1–5** was used to evaluate the thermal stability of the samples (ESI,† Fig. S6–S10). Complexes **1** and **2** are stable up to 158.0 and 161.2 °C,

Open Access Article. Published on 17 April 2023. Downloaded on 8/9/2025 3:58:16 PM.
This article is licensed under a Creative Commons Attribution 3.0 Unported Licence.

respectively (ESI,† Fig. S6 and S7). At these temperatures, they start to release the four Isn ligands up to 264.2 °C (exp. 45.3%; calcd 45.9%) and 273.9 °C (exp. 42.5%; calcd 42.2%). Therefore, the thermal stability of complexes **1** and **2** is almost identical, which is in line with their isostructural arrangement. Complex **3** is stable up to 115.7 °C, where a weight loss of 28.3% (calcd 29.6%) attributed to the release of two 4-Acpy is observed (ESI,† Fig. S8). In **4**, a weight loss from 71.7 °C to 97.7 °C of 3.9% (calcd 3.0%) is assigned to the removal of a water molecule, while in **5** the weight loss between 75.7 °C and 112.6 °C of 6.1% (calcd 6.4%) is attributed to the release of three water molecules. From this point, complex **4** exhibits a sequential loss of two 4-Acpy ligands, the first between 97.7 °C and 172.6 °C (exp. 23.2%; calcd 20.4%) and then from 172.6 °C to 284.9 °C (exp. 20.0%; calcd 20.4%) (ESI,† Fig. S9). Instead, the TGA of complex **5** suggests a simultaneous loss of one 4-Acpy and two 2-FA ligands (exp. 40.9%; calcd 40.7%) accompanied by decomposition (ESI,† Fig. S10). Thus, the thermal stability of the complexes follows the order **4** < **5** < **3** < **1** < **2**.

The FTIR-ATR spectra of **1**–**5** display the characteristic bands of 2-FA and their corresponding dPy ligands. The absence of a strong band at 1674 cm^{-1} in all the compounds indicates that 2-FA is deprotonated. In addition, all the compounds display typical bands between 1574–1540 cm^{-1} for ν_{as}(COO) and 1420–1397 cm^{-1} for ν_s(COO), displaying a difference with values of 158 and 135 cm^{-1} (**1**), 158 and 146 cm^{-1} (**2**), 159 cm^{-1} (**3**), 127 cm^{-1} (**4**), 144 and 132 cm^{-1} (**5**) attributed to the Δ values, indicating bridged (**1**–**3**, **5**) and chelated (**1**, **2**, **4**, and **5**) coordination modes of the carboxylate groups.[44,45] Additionally, other bands such as the vibrations of the aromatic rings (ν(C=C/C=N) and δ(C=C/C=N)) from either 2-FA and the dPy ligands, or the carbonyl groups from dPy and the N–H vibrations from Isn, have also been identified and assigned.[46] Remarkably, compound **4** presents two ν(C=O) vibrations attributed to a slightly different behavior of their 4-Acpy ligands in comparison with **3** and **5**, which only show a single signal for ν(C=O). Compounds **4** and **5** also exhibit a broad band between 3330 and 3066 cm^{-1} attributed to ν(O–H) of solvent molecules (ESI,† Fig. S11–S15).

The ^{1}H and ^{13}C{^{1}H} NMR spectra of **1**–**5** were recorded in DMSO-d_6. All the spectra show the signals of 2-FA and their corresponding dPy ligands. The ^{1}H NMR spectra of all the compounds present three signals between 7.76 and 6.51 ppm assigned to the protons of 2-FA. For **1** and **2**, the aromatic H atoms from Isn are observed between 8.83 and 7.76 ppm, while the bands attributable to the amide group H atoms are found at 8.25, 7.76 (**1**), and 8.23, 7.69 ppm (**2**). Otherwise, the aromatic H atoms of 4-Acpy in **3**–**5** appear between 8.83 and 7.81 ppm. Moreover, the signal of the methyl group from 4-Acpy is found around 2.62 ppm. The ^{1}H NMR spectra of **1**–**5** confirm the 1 : 1 (**1**, **2**, **4**), 2 : 1 (**3**) and 4 : 1 (**5**) molar ratio between 2-FA and the corresponding dPy ligand (ESI,† Fig. S16–S20).

In the ^{13}C{^{1}H} NMR spectra, the signals corresponding to the carboxylate group of 2-FA are found between 164.6 and 163.7 ppm, while those corresponding to the carbon atoms from the five-membered ring appear between 144.9 and 111.4 ppm. Regarding the dPy ligands, the signal from the carbonyl group of 4-Acpy in **3**–**5** (~198 ppm) is downfield shifted with respect to the carbonyl of Isn in **1** and **2** (~166 ppm). In addition, the aromatic carbon atoms appeared between 150.9 and 121.4 ppm, while the methyl carbon atoms of 4-Acpy are shown around 27 ppm in **3**–**5** (ESI,† Fig. S21–S26).[46] The correct assignment of the C aromatic atoms required the use of a DEPT-135 experiment (ESI,† Fig. S23).

Crystal structure of compounds 1 and 2

Compounds **1** and **2** crystallize in the monoclinic $P2_1/c$ space group. Both are isostructural compounds consisting of a dimeric complex with [MO_4N_2] cores (M = Zn(II) (**1**), Cd(II) (**2**)) composed of two μ_2-η^1:η^1-2-FA, which join together the metal ions as well as two μ_2-η^2-2-FA and two μ_1-η^1-Isn ligands, forming distorted octahedral geometries (S = 6.229 (**1**), 3.807 (**2**)) (Fig. 2; ESI,† Table S1, Fig. S1 and S2), giving rise to [$M_2(CO_2)_4$]-2 + 2 SBUs. In addition, the bond lengths and

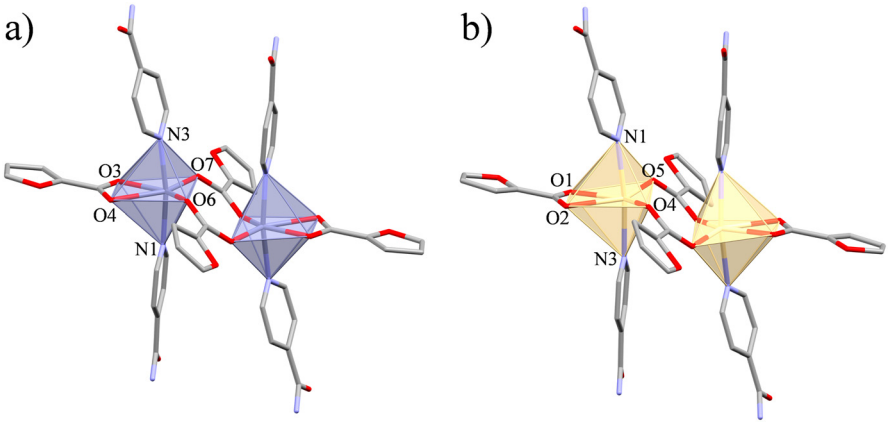

Fig. 2 Molecular structure of (a) **1** and (b) **2**. Hydrogen atoms have been omitted for clarity.

Open Access Article. Published on 17 April 2023. Downloaded on 8/9/2025 3:58:16 PM.
This article is licensed under a Creative Commons Attribution 3.0 Unported Licence.

Table 3 Bond lengths (Å) and bond angles (°) present in complexes **1** and **2**

1			
Bond lengths (Å)			
Zn(1)–O(3)	2.220(3)	Zn(1)–N(1)	2.144(4)
Zn(1)–O(4)	2.295(3)	Zn(1)–N(3)	2.148(3)
Zn(1)–O(6)	2.020(3)	Zn(1)···Zn(1)	3.9286(8)
Zn(1)–O(7)#1	2.015(3)		
Bond angles (°)			
O(3)–Zn(1)–O(4)	58.48(10)	O(4)–Zn(1)–N(3)	86.55(12)
O(3)–Zn(1)–O(6)	149.39(11)	O(6)–Zn(1)–O(7)#1	118.36(12)
O(3)–Zn(1)–O(7)#1	91.51(11)	O(6)–Zn(1)–N(1)	93.93(13)
O(3)–Zn(1)–N(1)	88.77(12)	O(6)–Zn(1)–N(3)	88.25(13)
O(3)–Zn(1)–N(3)	84.88(12)	O(7)#1–Zn(1)–N(1)	96.52(12)
O(4)–Zn(1)–O(6)	91.39(11)	O(7)#1–Zn(1)–N(3)	90.22(13)
O(4)–Zn(1)–O(7)#1	149.98(11)	N(1)–Zn(1)–N(3)	170.86(14)
O(4)–Zn(1)–N(1)	84.52(12)		
2			
Bond lengths (Å)			
Cd(1)–O(1)	2.358(3)	Cd(1)–N(1)	2.338(4)
Cd(1)–O(2)	2.436(3)	Cd(1)–N(3)	2.288(4)
Cd(1)–O(4)	2.193(4)	Cd(1)···Cd(1)	3.8337(7)
Cd(1)–O(5)#1	2.225(4)		
Bond angles (°)			
O(1)–Cd(1)–O(2)	54.37(11)	O(2)–Cd(1)–N(3)	87.42(12)
O(1)–Cd(1)–O(4)	145.32(14)	O(4)–Cd(1)–O(5)#1	124.35(15)
O(1)–Cd(1)–O(5)#1	89.51(14)	O(4)–Cd(1)–N(1)	87.23(15)
O(1)–Cd(1)–N(1)	86.36(13)	O(4)–Cd(1)–N(3)	92.06(14)
O(1)–Cd(1)–N(3)	89.86(12)	O(5)#1–Cd(1)–N(1)	88.47(15)
O(2)–Cd(1)–O(4)	91.12(13)	O(5)#1–Cd(1)–N(3)	98.28(14)
O(2)–Cd(1)–O(5)#1	143.55(13)	N(1)–Cd(1)–N(3)	172.24(14)
O(2)–Cd(1)–N(1)	84.86(13)		

(**1**) #1: $-x + 1, -y + 2, -z + 1$. (**2**) #1: $-x + 1, -y, -z + 1$.

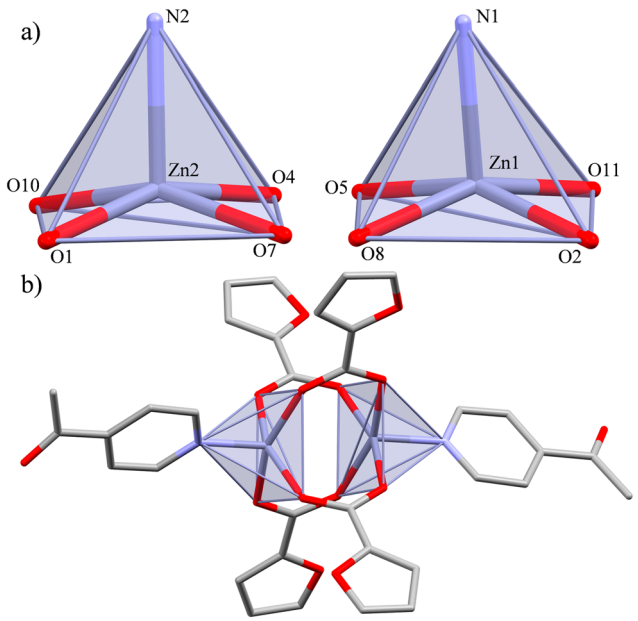

Fig. 3 Representation of (a) the [ZnO_4N] cores and (b) the dimeric paddle-wheel arrangement in **3**. Hydrogen atoms have been omitted for clarity.

Table 4 Bond lengths (Å) and bond angles (°) present in complex **3**

Bond lengths (Å)			
Zn(1)–O(2)	2.042(3)	Zn(2)–O(1)	2.008(3)
Zn(1)–O(5)	2.080(3)	Zn(2)–O(4)	2.045(3)
Zn(1)–O(8)	2.034(3)	Zn(2)–O(7)	2.063(3)
Zn(1)–O(11)	2.016(3)	Zn(2)–O(10)	2.073(3)
Zn(1)–N(1)	2.029(3)	Zn(2)–N(2)	2.031(3)
Zn(1)···Zn(2)	2.9875(5)		
Bond angles (°)			
O(2)–Zn(1)–O(5)	157.72(11)	O(1)–Zn(2)–O(4)	159.68(11)
O(2)–Zn(1)–O(8)	88.69(12)	O(1)–Zn(2)–O(7)	88.79(11)
O(2)–Zn(1)–O(11)	87.85(11)	O(1)–Zn(2)–O(10)	89.26(12)
O(2)–Zn(1)–N(1)	103.50(11)	O(1)–Zn(2)–N(2)	101.87(11)
O(5)–Zn(1)–O(8)	87.84(11)	O(4)–Zn(2)–O(7)	87.46(11)
O(5)–Zn(1)–O(11)	87.67(11)	O(4)–Zn(2)–O(10)	86.85(11)
O(5)–Zn(1)–N(1)	98.77(10)	O(4)–Zn(2)–N(2)	98.45(11)
O(8)–Zn(1)–O(11)	159.28(11)	O(7)–Zn(2)–O(10)	158.16(11)
O(8)–Zn(1)–N(1)	96.98(11)	O(7)–Zn(2)–N(2)	101.28(10)
O(11)–Zn(1)–N(1)	103.69(11)	O(10)–Zn(2)–N(2)	100.40(11)

bond angles oscillate between 2.015(3)–2.295(3) Å and 58.48(10)–170.86(14)° (**1**), and 2.193(4)–2.436(3) Å and 54.37(11)–172.24(14)° (**2**), lying within the range of previously reported dimeric compounds (Table 3).[11]

Crystal structure of compound 3

Compound **3** crystallizes in the tetragonal $P4_3$ space group bearing a [$Zn_2(CO_2)_4$] dimeric paddle-wheel Zn(II) array holding two [ZnO_4N] cores with a slightly distorted square pyramidal geometry (S = 0.199 for Zn(1), 0.175 for Zn(2)) (Fig. 3a and Table S1, ESI†). This arrangement is assembled by four μ^2-η^1:η^1 carboxylate ligands in a *syn–syn* conformation and two μ_1–η^1-4-Acpy ligands at the apical sites (Fig. 3b). The Zn–O bond lengths range between 2.008(2) and 2.080(3) Å, while the Zn–N bond lengths are between 2.029(3) and 2.031(3) Å (Table 4). These values are in range with those of previously reported paddle-wheel structures (2.009(1)–2.085(3)).[47–49] Finally, Zn(II) ions are displaced by 0.374 Å out of the basal plane towards the apical position.

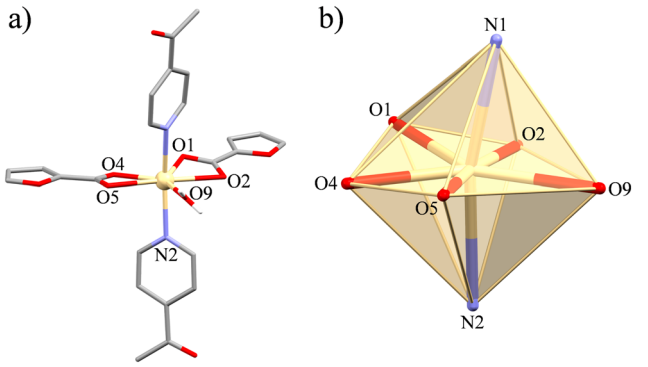

Fig. 4 (a) Monomeric structure of **4**. (b) Representation of its [CdO_5N_2] core. Hydrogen atoms have been omitted for clarity.

 This journal is © The Royal Society of Chemistry 2023

Open Access Article. Published on 17 April 2023. Downloaded on 8/9/2025 3:58:16 PM.
This article is licensed under a Creative Commons Attribution 3.0 Unported Licence.

Table 5 Bond lengths (Å) and bond angles (°) present in complex **4**

Bond lengths (Å)			
Cd(1)–O(1)	2.333(2)	Cd(1)–O(9)	2.284(2)
Cd(1)–O(2)	2.537(2)	Cd(1)–N(1)	2.361(3)
Cd(1)–O(4)	2.324(2)	Cd(1)–N(2)	2.356(3)
Cd(1)–O(5)	2.553(2)		
Bond angles (°)			
O(1)–Cd(1)–O(2)	53.81(8)	O(4)–Cd(1)–O(5)	53.63(8)
O(1)–Cd(1)–O(4)	82.19(8)	O(4)–Cd(1)–O(9)	139.19(9)
O(1)–Cd(1)–O(5)	134.02(8)	O(4)–Cd(1)–N(1)	97.87(9)
O(1)–Cd(1)–O(9)	138.58(9)	O(4)–Cd(1)–N(2)	90.66(9)
O(1)–Cd(1)–N(1)	90.40(9)	O(5)–Cd(1)–O(9)	86.14(8)
O(1)–Cd(1)–N(2)	100.88(9)	O(5)–Cd(1)–N(1)	84.45(8)
O(2)–Cd(1)–O(4)	134.50(8)	O(5)–Cd(1)–N(2)	92.54(8)
O(2)–Cd(1)–O(5)	171.86(7)	O(9)–Cd(1)–N(1)	83.02(9)
O(2)–Cd(1)–O(9)	85.75(8)	O(9)–Cd(1)–N(2)	83.87(9)
O(2)–Cd(1)–N(1)	93.82(8)	N(1)–Cd(1)–N(2)	166.71(9)
O(2)–Cd(1)–N(2)	87.34(8)		

Crystal structure of compound 4

Compound **4** crystallizes in the triclinic $P\bar{1}$ space group, displaying a monomeric array with a $[CdO_5N_2]$ core formed by two asymmetrically coordinated μ_1–η^2-2-FA ligands, two μ_1–η^1-4-Acpy and one μ_1–η^1 water molecule (Fig. 4a), showing a distorted pentagonal bipyramidal geometry (S = 2.773) (Fig. 4b and Table S1, ESI†). Its bond lengths and bond angles range between 2.284(2) and 2.553(2) Å, in agreement with similar Cd(II) monomeric structures (Table 5).[50,51]

Crystal structure of compound 5

Compound **5** crystallizes in the monoclinic $P2_1$ space group, accommodating two different polymeric chains (A and B). Chain A contains a $[CdO_6]$ core bearing a distorted trigonal prismatic geometry (S = 2.895; ESI,† Table S1) from two μ_2–η^1:η^1-*syn–anti*-2-FA ligands, one μ_1:η^2-2-FA and two water molecules (Fig. 5a), whereas chain B holds a $[CdO_6N]$ core with a slightly distorted pentagonal bipyramidal geometry (S = 1.210; ESI,† Table S1) from two different coordination modes of the 2-FA ligands (μ_2–η^2:η^1:η^1 and μ_1:η^1), a μ_1–η^1-4-Acpy ligand and a water molecule (Fig. 5b). Interestingly, the bridging bis-chelate (μ_2–η^2:η^1: η^1) coordination mode of the 2-FA ligand in chain B is quite unusual and seems to be modulated by the coordination of water molecules, which force geometric constraints through intra- and intermolecular

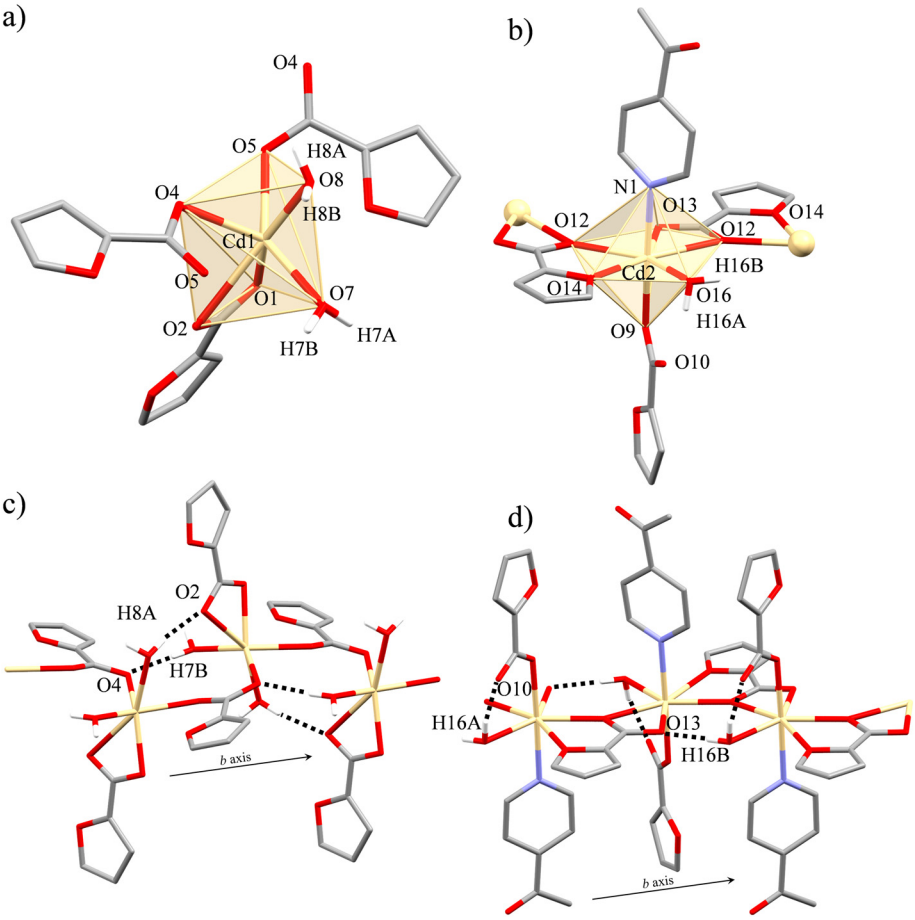

Fig. 5 Representation of the cores of (a) chain A and (b) chain B of **5**, and intramolecular interactions (black dashed lines) in (c) A and (d) B. Hydrogen atoms not involved in the interactions have been omitted for clarity.

Open Access Article. Published on 17 April 2023. Downloaded on 8/9/2025 3:58:16 PM.
This article is licensed under a Creative Commons Attribution 3.0 Unported Licence.

Table 6 Bond lengths (Å) and bond angles (°) present in complex **5**

Bond lengths (Å)			
Cd(1)–O(1)	2.270(3)	Cd(2)–O(9)	2.241(3)
Cd(1)–O(2)	2.633(4)	Cd(2)–O(12)	2.309(3)
Cd(1)–O(4)	2.271(3)	Cd(2)–O(12)#2	2.502(3)
Cd(1)–O(5)#1	2.297(3)	Cd(2)–O(13)#2	2.361(3)
Cd(1)–O(7)	2.258(3)	Cd(2)–O(14)	2.621(3)
Cd(1)–O(8)	2.310(3)	Cd(2)–O(16)	2.317(3)
		Cd(2)–N(1)	2.306(3)
Bond angles (°)			
O(1)–Cd(1)–O(2)	52.52(12)	O(9)–Cd(2)–O(14)	93.10(11)
O(1)–Cd(1)–O(4)	114.28(12)	O(9)–Cd(2)–O(16)	92.24(12)
O(1)–Cd(1)–O(5)#1	90.84(14)	O(9)–Cd(2)–N(1)	178.31(16)
O(1)–Cd(1)–O(7)	95.80(14)	O(12)–Cd(2)–O(12)#2	135.55(5)
O(1)–Cd(1)–O(8)	154.04(12)	O(12)–Cd(2)–O(13)#2	82.10(11)
O(2)–Cd(1)–O(4)	80.32(12)	O(12)–Cd(2)–O(14)	65.67(10)
O(2)–Cd(1)–O(5)#1	125.32(11)	O(12)–Cd(2)–O(16)	138.03(11)
O(2)–Cd(1)–O(7)	86.52(12)	O(12)–Cd(2)–N(1)	88.66(13)
O(2)–Cd(1)–O(8)	151.18(11)	O(12)#2–Cd(2)–O(13)#2	53.81(10)
O(4)–Cd(1)–O(5)#1	81.60(11)	O(12)#2–Cd(2)–O(14)	157.91(10)
O(4)–Cd(1)–O(7)	127.46(11)	O(12)#2–Cd(2)–O(16)	85.82(10)
O(4)–Cd(1)–O(8)	87.32(11)	O(12)#2–Cd(2)–N(1)	87.58(13)
O(5)#1–Cd(1)–O(7)	142.53(11)	O(13)#2–Cd(2)–O(14)	147.77(10)
O(5)#1–Cd(1)–O(8)	77.72(11)	O(13)#2–Cd(2)–O(16)	139.63(11)
O(7)–Cd(1)–O(8)	80.50(12)	O(13)#2–Cd(2)–N(1)	91.92(12)
O(9)–Cd(2)–O(12)	92.89(13)	O(14)–Cd(2)–O(16)	72.47(11)
O(9)–Cd(2)–O(12)#2	91.78(12)	O(14)–Cd(2)–N(1)	86.92(13)
O(9)–Cd(2)–O(13)#2	88.97(11)	O(16)–Cd(2)–N(1)	86.15(13)
Cd(2)–O(12)–Cd(2)#4	144.80(14)		

#1: $-x + 1, y - 1/2, -z$. #2: $-x + 2, y - 1/2, -z + 1$. #4 $-x + 2, y + 1/2, -z + 1$.

interactions. The Cd–O bond lengths with 2-FA ligands are within the range of previously reported Cd(II) complexes (2.218(3) for monodentate, 2.297(3)–2.361(3) Å for bridging, 2.1735(12)–2.3168(12), and 2.313(3)–2.499(3) for chelate).[52,53] Selected bond lengths and angles are displayed in Table 6.

The presence of coordinated water molecules promoted O–H···O interactions with carboxylate ligands and supported both the chain formation and the assembly of the chains. Two intramolecular interactions are held within chain A between H(7B) and H(8A) with O(4) and O(2), respectively (Fig. 5c). Likewise, H(16A) and H(16B) interact with O(10) and O(13) along chain B (Table 7 and Fig. 5d). Intramolecular interactions subtracted carboxylate O atoms and promoted the elongation of the corresponding Cd–O bond lengths. In A, the Cd(1)–O(2) bond length of μ_1:η^2-2-FA increases up to 2.634(4) Å, while in B the Cd(2)–O(13) bond length in μ_2:η^2:η^1: η^1-2-FA is lengthened to 2.361(3) Å (Table 6). Indeed, probably both H(16B) by an intramolecular interaction and H(7A) through an intermolecular association triggered the μ_1:η^1 coordination mode of 2-FA by grabbing the carboxylate O(10) atom. The presence of strong intramolecular interactions between coordinated water molecules and carboxylate O atoms has already fostered monodentate coordination modes in Cd(II) complexes.[53,54]

Table 7 Intramolecular interactions present in complex **5**

Intramolecular interactions in A	D–H (Å)	H···A (Å)	D···A (Å)	>D–H···A (°)
O(7)–H(7B)···O(4)	0.80(3)	1.93(3)	2.729(4)	177(5)
O(8)–H(8A)···O(2)	0.81(4)	1.93(4)	2.719(5)	168(4)
Intramolecular interactions in B	**D–H (Å)**	**H···A (Å)**	**D···A (Å)**	**>D–H···A (°)**
O(16)–H(16A)···O(10)	0.80(4)	1.86(4)	2.645(4)	168(6)
O(16)–H(16B)···O(13)	0.81(3)	1.91(3)	2.712(5)	178(6)

A detailed description of the extended structures as well as their associated distances and angles is provided in the ESI,† Fig. S27 and Table S2 (**1** and **2**), Fig. S28 and Table S3 (**3**), Fig. S29 and Table S4 (**4**), and Fig. S30 and Table S5 (**5**).

Photophysical properties

UV-vis spectroscopy. The UV-vis spectra of Isn and 4-Acpy ligands and complexes **1**–**4** were recorded in MeOH (99.8%), whereas those of 4-Acpy and **5** were measured in ACN (HPLC grade) at 298 K. To ensure non-aggregation of the ligands (ESI,† Fig. S31–S35) and the complexes (ESI,† Fig. S36–S40), we performed additive measurements between $\sim 1 \times 10^{-9}$ M and $\sim 1 \times 10^{-5}$ M in MeOH or ACN when required. In addition, a comparison between the absorption spectra of the ligands (ESI,† Fig. S41) and the complexes (ESI,† Fig. S42) at the selected concentration for the emission experiments is provided in the ESI.† The complexes display absorptions with an increasing intensity following the order **4** < **5** < **2** < **3** < **1**

Open Access Article. Published on 17 April 2023. Downloaded on 8/9/2025 3:58:16 PM.
This article is licensed under a Creative Commons Attribution 3.0 Unported Licence.

Table 8 Detailed parameters extracted from the photophysical properties of **1**–**5**[b]

Compound	$\lambda_{max\text{-}abs}$ (log(ε))	λ_{exc}	$\lambda_{max\text{-}em}$	Stokes shift	Φ_s
1	202 (4.60), 226 (4.60), 275 (4.01), 281 (3.84)	227	334, 345	14 113, 15 067	0.02
2	204 (6.87), 247 (6.43), 278 (5.75)	230	347, 364, 387	14 660, 16 006, 17 638	0.01
3	202 (7.20), 226 (6.69), 274 (5.94), 281 (5.90)	281	343	6433	0.43
4	207 (4.22), 278 (3.57)	281	334	5647	0.20
5	190[a] (4.74), 227 (4.74), 275 (3.75)	281	397, 419	10 398, 11 721	0.03

[a] Absorption maxima is out of range and the data of the highest energy peak is provided. [b] All the wavelengths are given in nm. ε values are given in $M^{-1} \times cm^{-1}$. Stokes shift values are given in cm^{-1}. $\lambda_{max\text{-}abs}$ = maximum of absorption; λ_{exc} = excitation maximum; $\lambda_{max\text{-}em}$ = maximum of emission; Φ_s = relative quantum yield of the samples using L-tyr as the standard (Φ = 0.14).[58]

at the selected concentrations. All the relevant details of the complexes are summarized in Table 8, while those from the ligands are provided in the ESI,† Table S6. From these data, it can be inferred that diluted samples of ~1 × 10^{-9} M solutions of complexes **1** and **2** show two bands centered at 202 and 227 nm (**1**) and 204 and 242 nm (**2**); upon concentration, any significant change is observable until ~1 × 10^{-7} M, where a progressive bathochromic shift was observed, suggesting aggregation (ESI,† Fig. S36 and S37). Compounds **3** and **4** present two defined bands centered at 202 and 281 nm (**3**) and 205 and 282 nm (**4**) at the initial concentration of ~1 × 10^{-9} M, while two additional bands overlapped the first one arising at 222 and 242 nm (**3**) and 219 and 242 nm (**4**) after the concentration is increased. Since a noticeable shift of the bands as in **1** and **2** was not observed when the concentration was increased, no apparent signals of aggregation of **3** and **4** were observed (ESI,† Fig. S38 and S39). Finally, the UV-vis spectrum of **5** presents a main signal centered at 242 nm together with an overlapped signal around 219 nm and a minor one at 281 nm. The spectrum does not show any aggregation evidence upon concentration as for complexes **3** and **4** (ESI,† Fig. S40). Hence, it seems that compounds presenting Isn (**1** and **2**) are more prone to present aggregation than complexes containing 4-Acpy (**3**–**5**) as ligands, which could be attributed to the strong preference of the Isn ligands towards the formation of amide–amide homosynthons between their amide moieties, in contrast to 4-Acpy, which does not present any recurrent supramolecular synthon.[55,56] Therefore, solutions of ~1 × 10^{-8} M were selected for **1**–**5** to measure their photoluminescence properties, aiming to prevent negative effects derived from aggregation-caused quenching (ACQ).[57] In addition, the UV-vis absorption spectra of each complex have been compared to those of the corresponding ligands at the concentration used for the emission experiments (ESI,† Fig. S43–S47).

It seems that the photophysical properties of the complexes can be understood by extrapolating the results from previously reported analogous complexes.[11] In these studies, the origin of the less energetic transitions in the absorption spectra of Zn(II) and Cd(II) complexes was found to be ligand centered (LC) over the carboxylate ligands regardless of the structure with only contribution from LC transitions over 4-Acpy, whereas Isn excitation in the complexes occurs at lower wavelengths. Moving to higher energies, these transitions become dependent on the molecular structure and the electronic properties of the dPy ligands. In line with these results, absorption maxima at 275 and 281 nm (**1**, ESI,† Fig. S43) and 278 nm (**2**, ESI,† Fig. S44) could be ascribed to 2-FA LC transitions, whereas absorption at 281 nm (**3**, ESI,† Fig. S45) and 278 nm (**4**, ESI,† Fig. S46) probably originates from a mixture of 2-FA and 4-Acpy LC transitions. Mimicking previous results, the Isn ligand seems to promote intraligand charge transfer (ILCT) transitions between 220 and 250 nm supported by the dimeric arrangement, while complexes with 4-Acpy display only LC transitions, especially in the dimeric paddle-wheel complex that displays the worst arrangement for charge transfers between dPy ligands. Indeed, the origin of the absorptions at 226 nm (**1**) and 247 nm (**2**) was attributed to ILCT between Isn ligands since these bands were not observed for the free ligands in MeOH (202 and 271 nm for 2-FA, and 202 and 274 nm for Isn) and fall within the mentioned range for Isn complexes. In the case of **5**, from the absorption spectra of the ligands in ACN, the assignment of the absorption band at 275 nm to a 4-Acpy LC transition seems more reasonable, perhaps with a small contribution from 2-FA even if its absorption in this region is meager (ESI,† Fig. S47).

Therefore, the absorption of the complexes can be attributed to local excitations (LEs) of 2-FA and dPy ligands in **3**–**5**, with the contribution of ILCT between Isn ligands in **1** and **2**. Since the incorporation of a better electron-withdrawing group in *para* position should be reflected as a bathochromic shift in absorption, complexes with 4-Acpy ligand display absorption maxima at lower energy than those with Isn.

Fluorescence spectroscopy. Fluorescence measurements were performed using MeOH (99.8%) for **1**–**4** and ACN (HPLC grade) for **4** and **5**, whereas DRST studies of **4** were conducted in ACN (≥99.5%). Complexes **1** and **2** show unfolded emission bands presenting their maxima at 334, 345 nm (**1**) and 347, 364, 387 nm (**2**) when excited at 227 and 230 nm, respectively. Differently, compounds **3**–**5** were excited at 281 nm, displaying single bands centered at 343 nm (**3**) and 334 nm (**4**), while compound **5** showed an unfolded signal with two apparent peaks at 397 and 419 nm (Table 8 and Fig. 6).

The wavelength of the emission maxima of the compounds containing Isn (λ_{exc} = 227 nm, **1**; 230 nm, **2**) is hypsochromically shifted compared to that of the compounds

Open Access Article. Published on 17 April 2023. Downloaded on 8/9/2025 3:58:16 PM.
This article is licensed under a Creative Commons Attribution 3.0 Unported Licence.

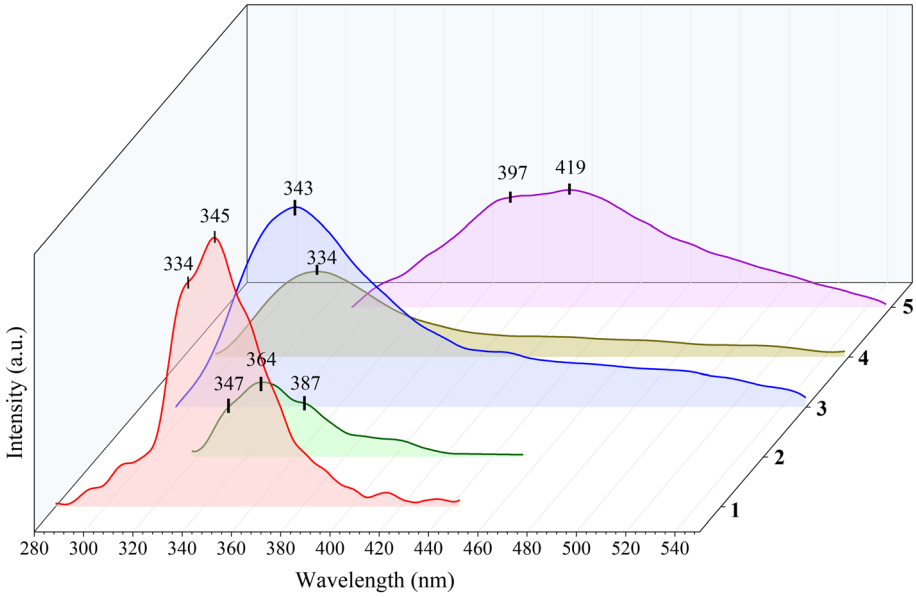

Fig. 6 Emission spectra of complexes **1**–**5** excited at 227 nm (**1**), 230 nm (**2**) and 281 nm (**3**–**5**) using MeOH (**1**–**4**) and ACN (**5**) solutions of ~1 × 10^{-8} M.

containing 4-Acpy (λ_{exc} = 281 nm, **3**–**5**). In addition, the emission of each complex has been compared with their corresponding ligands at the same λ_{exc}, observing a bathochromic shift of the bands in complexes **1**–**3** and **5**, whereas compound **4** shows a hypsochromic shift with respect to the emission of 2-FA (ESI,† Fig. S48–S52). Furthermore, according to the CIE 1931 chromaticity diagram, the resultant emission colors are electric violet (**1** and **2**), azure radiance (**3** and **4**), and blue ribbon (**5**) (ESI,† Fig. S53).

The relative quantum yields (Φ_s) of **1**–**5** were calculated using eqn (1):

$$\Phi_s = \Phi_{ref} \times \left(\frac{OD_{ref}}{OD_s}\right) \times \left(\frac{I_S}{I_{ref}}\right) \times \left(\frac{n_s}{n_{ref}}\right)^2 \quad (1)$$

where Φ_s is the quantum yield, OD is the optical density (or absorbance) at the selected excitation wavelength, I is the area under the curve of the emission spectra, and n is the refractive index of the employed solvent. L-Tyrosine was utilized as reference (Φ_{ref} = 0.14),[58] using 1.01 × 10^{-7} M solutions with Milli-Q water (n = 1.3325),[59] while samples **1**–**4** were measured in MeOH (n = 1.3314),[60] and compound **5** in ACN (n = 1.3404),[61] all of them at 298 K. The resulting Φ_s values were 0.02 (**1**), 0.01 (**2**), 0.43 (**3**), 0.20 (**4**), and 0.03 (**5**). The lower quantum yields of compounds **1** and **2** should be tentatively attributed to the probable rotation of their amide moieties towards the formation of intramolecular amide–amide homosynthons, leading to charge transfers between Isn ligands that should decrease the resulting fluorescence efficiencies.[11,62] Moreover, the coordination of water molecules in **4** and **5** is also ascribed to a quenching of their fluorescence quantum yields, providing additional pathways to non-radiative decay processes as more water molecules are coordinated to the metal centers.[63–65] Finally, compound **3** possesses a higher Φ_s, which should be related to the paddle-wheel motif that minimizes charge transfer transitions between the 4-Acpy and the 2-FA ligands compared with the arrays of the rest of the compounds.[11]

Insights into the DRST process

The formation of the M–O bond from the furane ring in complexes **1**–**4** seems to be hindered by the saturated coordination environment of Zn(II) and Cd(II) ions *via* the preferred coordination of the carboxylate O atoms and N-donor ligands in MeOH. The H-bond ability of MeOH can promote O–H···O interactions with the furane O atom and displace its coordination. Hence, we selected complex **4** as a suitable candidate for the DRST experiment considering two premises: (i) that heptacoordinate geometry presents remarkable degrees of geometrical distortions and (ii) Cd(II) ions can accommodate high coordination numbers up to eight.

Indeed, heptacoordinate geometries hold small energetic differences between the primary accessible polyhedral: the capped octahedral (COC-7), the capped trigonal prismatic (CTPR-7), and the pentagonal bipyramidal (PBPY-7)[66–68] and are prone to be intermediates of six- and eight-coordinated complexes from associative or dissociative reactions.[69] These small differences are associated with low-barrier fluxional processes that foster stereochemical modifications and interconversion through small angular displacement. Instead, the greater stability of a hexacoordinated Cd(II) complex was reported to exhibit small geometrical changes without variation in the coordination bonds.[70]

Open Access Article. Published on 17 April 2023. Downloaded on 8/9/2025 3:58:16 PM.
This article is licensed under a Creative Commons Attribution 3.0 Unported Licence.

In complex **4**, the 4-Acpy ligands are located at the apical sites of the pentagonal bipyramid and thus are prone to be exchanged. It should be stressed that surrounding O atoms from carboxylate groups, even if not directly coordinated to the Cd(II) center, participate in the interconversion between the polyhedra by imposing geometrical constraints. Initially, in the structure of **4**, the coordinated water molecule orients the furane O atoms of vicinal monomers towards the Cd(II) ion. The incorporation of a second water molecule led to the full dissociation of 4-Acpy ligands resulting in chain *A* formation. Therefore, we could understand chain B of **5** as an intermediate arrangement of a DRST process in which **4** suffers an apical site ligand exchange between 4-Acpy and water molecules to yield chain A. The co-crystallization of chain B seems to be grounded by the five-membered ring stabilization after the coordination of the furane O atom. There are three potential mechanisms for ligand substitution: associative, dissociative, or interchange, and in particular, interchange can retain the metal coordination environment or present products from association or dissociation.[21] In this example, the DRST process induces a dissociative interchange since the bond formation and breaking results in a lower coordination number.[21] In line with this statement, the reaction of 2-FA with Cd(II) in water promoted the coordination of an additional water molecule, increasing the coordination number to seven and yielding the monomer $[Cd(2\text{-FA})(OH_2)_3]$ with three coordinated water molecules.[71]

As aforementioned, study of the changes in the properties of the complexes involved in DRST processes has not been extensively pursued. Most of the cases provide structural data about the initial and the final product,[28,72] but fewer examples present tracing of the DRST and factors governing the transformation. From the limited number of examples, Zhang *et al.* demonstrated the importance and potential interest of water-induced DRST processes in a series of Cu(I)-based arrays. Indeed, they were able to trace the interconversion process by fluorescence spectroscopy, which resulted in a decrease of the Φ_s without a significant shift in emission maxima.[36]

To ensure the role of both the solvent and the presence of water molecules, we conducted fluorescence experiments to follow the structural transformation between **4** and **5**. We therefore recorded the emission spectra of **4** in ACN (HPLC grade) using a concentration of $\sim 1 \times 10^{-3}$ M without observing changes when compared with the spectra of **4** in MeOH. Considering that no structural transformation seems to occur under these conditions and that the difference between the emission of **4** and **5** in ACN (HPLC grade) is reflected as a bathochromic shift of 85 nm and a decrease of the Φ_s, fluorescence proved to be a useful technique to trace the interconversion between **4** and **5**.

Then, the spectrum of **4** in ACN (≥99.5%) was monitored over time. At a concentration of $\sim 1 \times 10^{-3}$ M, the initial $t = 0$ min measurement resulted in the rising of an emission band at the same position of **5** with a small shoulder from **4**, indicating a fast conversion from **4** to **5**. In less than three minutes this shoulder disappeared (Fig. 7a), suggesting a full conversion. Hence, to slow down the transformation from **4** to **5**, the same experiment was carried out using a more diluted sample ($\sim 1 \times 10^{-4}$ M). In this case, the initial measurement shows that **4** remains completely unaltered, while after three minutes a mixture of **4** and **5** has been identified, that continues the transformation until minute six (Fig. 7b). From this point forward, the process has been followed for two days without observing any significant change in emission, suggesting a partial structural transformation below 1×10^{-3} M in solution, being both **4** and **5** in coexistence. It should be noted that the recrystallization of **4** was conducted at higher concentrations of $\sim 1 \times 10^{-2}$ M and thus, the full conversion would be achieved, favoring the crystallization of **5**.

Therefore, the fluorescence experiments demonstrate that the DRST process requires both the use of a polar aprotic solvent, avoiding the formation of strong hydrogen bond

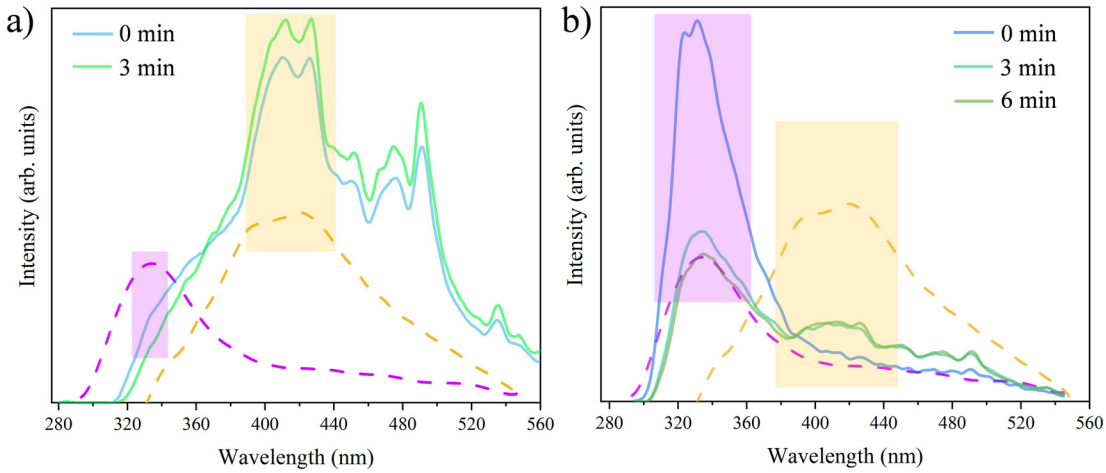

Fig. 7 Monitoring of the structural transformation of **4** to **5** in a concentration of (a) $\sim 1 \times 10^{-3}$ M and (b) $\sim 1 \times 10^{-4}$ M in 3 mL of ACN (≥99.5%). Purple dashed lines represent the emission spectra of **4** in MeOH (99.8%) at $\sim 1 \times 10^{-8}$ M, while orange dashed lines indicate the emission spectra of **5** in ACN (HPLC grade) at $\sim 1 \times 10^{-8}$ M.

Open Access Article. Published on 17 April 2023. Downloaded on 8/9/2025 3:58:16 PM.
This article is licensed under a Creative Commons Attribution 3.0 Unported Licence.

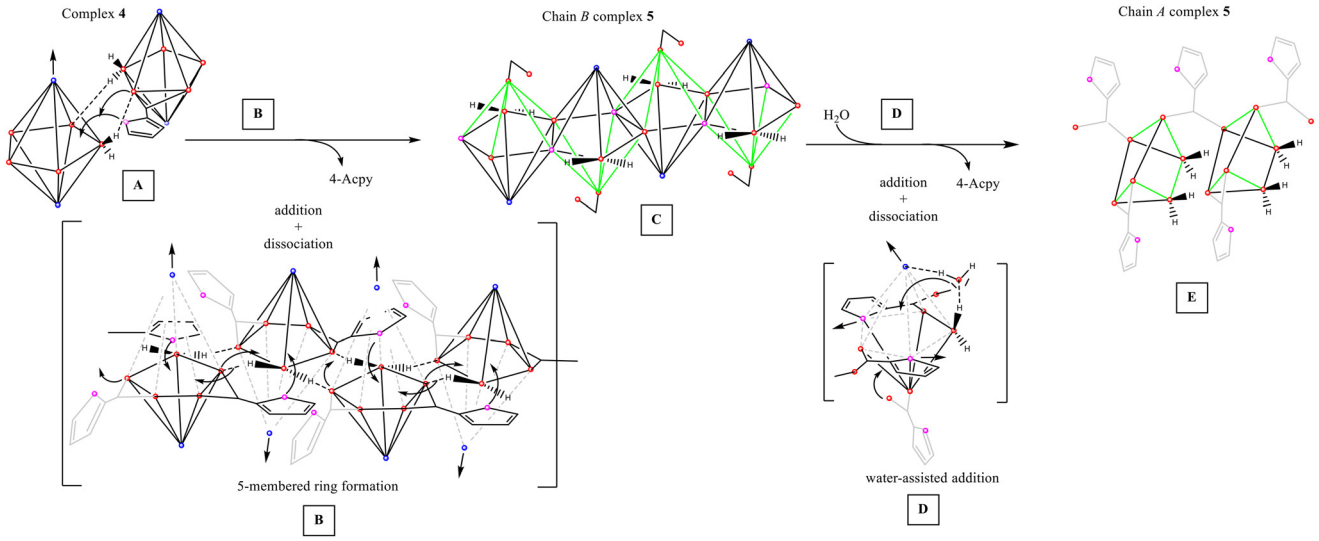

Scheme 2 Representation of the DRST pathway between **4** and **5**. Charts between brackets represent intermediate geometries. Green solid lines refer to newly formed edges by the addition or uncoordination of carboxylate moieties. Ligands in grey stand for non-chelating 2-FA. Straight black arrows indicate the release of the atom, whereas black curved arrows indicate addition of atoms.

interactions, and the presence of water that triggered the molecular rearrangement. Interestingly, this DRST process results in a significant change in the emission properties by both a change in the emission wavelength and a decrease in the fluorescence quantum yield.

After merging these results, our assumption is that the redissolution of **4** in a polar medium led to a geometric accommodation and the addition of the vicinal furane O atom from a neighboring monomeric unit already facing towards the Cd(II) ion by the mentioned H-bond (Scheme 2-A) that favors the release of one 4-Acpy ligand at the apical site. This spatial disposition is triggered by the strong O–H···O interactions from coordinated water molecules, so the addition of the furane ring is accomplished through the complementary face sharing the vertex with water in the PBPY-7 polyhedron. The additional stabilization of the five-membered ring formation seems to be enough to displace the 4-Acpy ligand and change the chelate coordination mode of 2-FA to monodentate, promoting polymerization of the monomeric units (Scheme 2-B). Again, coordinated water molecules shift to perform intramolecular H-bond interactions to stabilize the monodentate coordination mode. Once chain B of **5** is formed (Scheme 2-C), a water-assisted addition of another water molecule promotes the decoordination of the weak furane O atoms and the release of the remaining 4-Acpy. This is accompanied by a geometric accommodation of the coordination environment with the subsequent change in the coordination mode of the monodentate 2-FA to chelate (Scheme 2-D), ending in polymer chain A. The water-assisted addition of the second water molecule agrees with their allocation, both being at the same edge of the trigonal prismatic polyhedron (Scheme 2-E).

The role of solvent molecules in inducing rearrangements, changes or even cleavage of M–O carboxylate bonds has already been demonstrated and it seems to be required for the structural transformation.[21,27] Indeed, water holds 48% of the structural transformations involving changes in the coordination environment.[73] The key role of water within this DRST process is highlighted by the formation of strong intramolecular and intermolecular H-bond interactions. It assists in the change in coordination number of the Cd(II) center both by modulating the coordination or not of the carboxylate ligands through strong H-bond interactions and by promoting their geometric re-accommodation.

Conclusions

Five Zn(II)/Cd(II) complexes based on 2-FA and two different dPy ligands (Isn and 4-Acpy) have been successfully synthesized and characterized. We confirmed the structure-directed arrangement of the dimeric complexes (**1** and **2**) by the recurrent amide–amide homosynthon regardless of the monodentate carboxylic acid. Instead, the non-guiding 4-Acpy allows the formation of paddle-wheel (**3**) or monomeric (**4**) arrangements. Remarkably, the DRST of **4** in ACN leads to the formation of an unusual CP (**5**). This set of compounds displayed the whole range of coordination modes of 2-FA from monodentate to the unusual bridging bis-chelate, and variable coordination numbers between five and seven. The photophysical properties of all the compounds were recorded, observing better Φ_s values for the complexes containing 4-Acpy (**3**–**5**) with respect to Isn (**1** and **2**). Among them, the paddle-wheel motif seems to maximize its IL emission, displaying a Φ_s of 0.43. Conversely, the coordination of water molecules in **4** and **5** leads to a quenching of their fluorescence efficiency, while the amide–amide homosynthon of **1** and **2** could force a molecular motion in solution towards the formation of intramolecular

Open Access Article. Published on 17 April 2023. Downloaded on 8/9/2025 3:58:16 PM.
This article is licensed under a Creative Commons Attribution 3.0 Unported Licence.

amide–amide interactions and cause the strong reduction of Φ_s. Interestingly, the competitiveness between water, carboxylate, and a weakly coordinating O atom from a furane ring has been demonstrated by tracing the formation of **5** by a DRST process through X-ray data and fluorescence experiments. These results contribute to the limited number of cases in which DRST processes have been traced to date and evince the crucial role of solvents in controlling the engagement of weakly coordinating atoms, in particular of water molecules in the assembly of discrete molecular entities.

Author contributions

Conceptualization, J. P.; data curation, D. E., F. S.-F. and M. F.-B; formal analysis, D. E., F. S.-F. and M. F.-B; funding acquisition, J. P.; investigation, D. E. and F. S.-F.; methodology, D. E. and F. S.-F.; project administration, J. P.; resources, J. P. and T. C.; software, D. E. and F. S.-F.; supervision, J. P.; validation, J. P. and T. C.; visualization, D. E. and F. S.-F.; writing – original draft preparation, D. E. and F. S.-F.; writing – review and editing, J. P. and T. C. All authors have read and agreed to the published version of the manuscript.

Conflicts of interest

There are no conflicts to declare.

Acknowledgements

J. P. acknowledges financial support from the CB615921 project, the CB616406 project from "Fundació La Caixa", and the 2017SGR1687 project from the Generalitat de Catalunya. D. E. acknowledges the PIF predoctoral fellowship from the Universitat Autònoma de Barcelona.

References

1 A. N. Gusev, M. A. Kiskin, E. V. Braga, M. Chapran, G. Wiosna-Salyga, G. V. Baryshnikov, V. A. Minaeva, B. F. Minaev, K. Ivaniuk, P. Stakhira, H. Ågren and W. Linert, *J. Phys. Chem. C*, 2019, **123**, 11850–11859.
2 A. Gusev, V. Shul, E. Braga, E. Zamnius, M. Kryukova and W. Linert, *Dyes Pigm.*, 2020, **183**, 108626.
3 C. V. Esteves, J. Costa, H. Bernard, R. Tripier and R. Delgado, *New J. Chem.*, 2020, **44**, 6589–6600.
4 B. Dutta, A. Dey, C. Sinha, P. Pratim Ray and M. H. Mir, *Inorg. Chem.*, 2018, **57**, 8029–8032.
5 A. Chandra, M. Das, K. Pal, S. Jana, B. Dutta, P. P. Ray, K. Jana and C. Sinha, *ACS Omega*, 2019, **4**, 17649–17661.
6 J. Cepeda, S. Pérez-Yáñez, J. Á. García, S. Rojas and A. Rodríguez-Diéguez, *Dalton Trans.*, 2021, **50**, 9269–9282.
7 C. R. Groom, I. J. Bruno, M. P. Lightfoot and S. C. Ward, *Acta Crystallogr., Sect. B: Struct. Sci., Cryst. Eng. Mater.*, 2016, **72**, 171–179.
8 Y. Bing, X. Li, M.-Q. Zha and D.-J. Wang, *Synth. React. Inorg., Met.-Org., Nano-Met. Chem.*, 2011, **41**, 798–804.
9 A. E. Goldberg, M. A. Kiskin, S. A. Kozyukhin, A. A. Sidorov and I. L. Eremenko, *Russ. Chem. Bull.*, 2011, **60**, 1012–1015.
10 G.-B. Che, S.-S. Wang, X.-L. Zha, X.-Y. Li, C.-B. Liu, X.-J. Zhang, Z.-L. Xu and Q.-W. Wang, *Inorg. Chim. Acta*, 2013, **394**, 481–487.
11 F. Sánchez-Férez, J. M. Rius-Bartra, J. A. Ayllón, T. Calvet, M. Font-Bardia and J. Pons, *Molecules*, 2022, **27**, 1365.
12 G. Kumar, G. Kumar and R. Gupta, *Inorg. Chem. Front.*, 2021, **8**, 1334–1373.
13 D. Ejarque, F. Sánchez-Férez, J. A. Ayllón, T. Calvet, M. Font-Bardia and J. Pons, *Cryst. Growth Des.*, 2020, **20**, 383–400.
14 F. Sánchez-Férez, X. Solans-Monfort, T. Calvet, M. Font-Bardia and J. Pons, *CrystEngComm*, 2022, **24**, 4351–4355.
15 L. Zhang, Z.-J. Li, Q.-P. Lin, J. Zhang, P.-X. Yin, Y.-Y. Qin, J.-K. Cheng and Y.-G. Yao, *CrystEngComm*, 2009, **11**, 1934–1939.
16 C.-S. Liu, E. C. Sañudo, M. Hu, L.-M. Zhou, L.-Q. Guo, S.-T. Ma, L.-J. Gao and S.-M. Fang, *CrystEngComm*, 2010, **12**, 853–865.
17 C.-S. Liu, C. Wang, M. Hu and S.-M. Fang, *Z. Anorg. Allg. Chem.*, 2011, **637**, 748–754.
18 B. Paluchowska, J. K. Maurin and J. Leciejewicz, *J. Coord. Chem.*, 2001, **52**, 253–264.
19 P. Braunstein and F. Naud, *Angew. Chem., Int. Ed.*, 2001, **40**, 680–699.
20 L. Zhang, J. Zhang, Z.-J. Li, Y.-Y. Qin, Q.-P. Lin and Y.-G. Yao, *Chem. – Eur. J.*, 2009, **15**, 989–1000.
21 C.-P. Li and M. Du, *Chem. Commun.*, 2011, **47**, 5958–5972.
22 X. F. Zheng, X. Q. Shen, X. S. Wan, H. Y. Zhang, H. Wang, R. Yang and C. Y. Niu, *J. Coord. Chem.*, 2007, **60**, 1317–1325.
23 C.-C. Ai, J.-F. Xiang, M. Li and L.-J. Yuan, *Acta Crystallogr., Sect. E: Struct. Rep. Online*, 2007, **63**, m565–m566.
24 I. A. Lutsenko, D. E. Baravikov, M. A. Kiskin, Y. V. Nelyubina, P. V. Primakov, O. B. Bekker, A. V. Khoroshilov, A. A. Sidorov and I. L. Eremenko, *Russ. J. Coord. Chem.*, 2020, **46**, 411–419.
25 I. A. Lutsenko, D. S. Yambulatov, M. A. Kiskin, Y. V. Nelyubina, P. V. Primakov, O. B. Bekker, A. A. Sidorov and I. L. Eremenko, *Russ. J. Coord. Chem.*, 2020, **46**, 787–794.
26 W. Ai, H. He, L. Liu, Q. Liu, X. Lv, J. Li and D. Sun, *CrystEngComm*, 2008, **10**, 1480–1486.
27 D.-X. Xue, W.-X. Zhang, X.-M. Chen and H.-Z. Wang, *Chem. Commun.*, 2008, 1551–1553.
28 L.-H. Cao, H.-Y. Li, H. Xu, Y.-L. Wei and S.-Q. Zang, *Dalton Trans.*, 2017, **46**, 11656–11663.
29 A. Chaudhary, A. Mohammad and S. M. Mobin, *Cryst. Growth Des.*, 2017, **17**, 2893–2910.
30 Y. Li, B. Zhao, J.-P. Xue, J. Xie, Z.-S. Yao and J. Tao, *Nat. Commun.*, 2021, **12**, 6908.
31 F. F. Li, L. Zhang, L. Le Gong, C. S. Yan, H. Y. Gao and F. Luo, *Dalton Trans.*, 2017, **46**, 338–341.
32 M. Zhu, X.-Z. Song, S.-Y. Song, S.-N. Zhao, X. Meng, L.-L. Wu, C. Wang and H.-J. Zhang, *Adv. Sci.*, 2015, **2**, 1500012.
33 L.-H. Cao, Y.-S. Wei, H. Xu, S.-Q. Zang and T. C. W. Mak, *Adv. Funct. Mater.*, 2015, **25**, 6448–6457.
34 D.-L. Meng, X. Wang, C.-B. Tian, W. Wei and S.-W. Du, *Cryst. Growth Des.*, 2020, **20**, 1203–1210.

Open Access Article. Published on 17 April 2023. Downloaded on 8/9/2025 3:58:16 PM.
This article is licensed under a Creative Commons Attribution 3.0 Unported Licence.

35 X.-F. Zhang, T. Yan, T. Wang, J. Feng, Q. Wang, X. Wang, L. Du and Q.-H. Zhao, *CrystEngComm*, 2018, **20**, 570–577.
36 Z.-Y. Zhang, Y. Su, L.-X. Shi, S.-F. Li, F. Fabunmi, S.-L. Li, T. Yu, Z.-N. Chen, Z. Su and H.-K. Liu, *Inorg. Chem.*, 2020, **59**, 13326–13334.
37 L. Fan, X. Liu, L. Zhang, X. Kong, Z. Xiao, W. Fan, R. Wang and D. Sun, *J. Mol. Struct.*, 2019, **1197**, 87–95.
38 L. Moreno-Gómez, F. Sánchez-Férez, T. Calvet, M. Font-Bardia and J. Pons, *Inorg. Chim. Acta*, 2020, **506**, 119561.
39 W. Wang, Y.-X. Wang and H.-B. Yang, *Chem. Soc. Rev.*, 2016, **45**, 2656–2693.
40 G. M. Sheldrick, *Acta Crystallogr., Sect. A: Found. Crystallogr.*, 2008, **64**, 112–122.
41 C. F. MacRae, I. Sovago, S. J. Cottrell, P. T. A. Galek, P. McCabe, E. Pidcock, M. Platings, G. P. Shields, J. S. Stevens, M. Towler and P. A. Wood, *J. Appl. Crystallogr.*, 2020, **53**, 226–235.
42 *Persistence of Vision Pty. Ltd., Persistence of Vision (TM) Raytracer*, Williamstown, Australia, 2004, Available online: **https://www.povray.org/** (accessed on 12 April 2023).
43 M. Llunell, D. Casanova, J. Cirera, P. Alemany and S. Alvarez, *SHAPE. Program for the Stereochemical Analysis of Molecular Fragments by Means of Continuous Shape Measures and Associated Tools*, Universitat de Barcelona, Barcelona, 2013.
44 G. B. Deacon and R. J. Phillips, *Coord. Chem. Rev.*, 1980, **33**, 227–250.
45 K. Nakamoto, *Infrared and Raman Spectra of Inorganic and Coordination Compounds: Part A: Theory and Applications in Inorganic Chemistry*, Wiley Interscience, Hoboken, New Jersey, USA, 6th edn, 2009.
46 D. H. Williams and I. Fleming, *Spectroscopic Methods in Organic Chemistry*, Springer Nature, Cham, Switzerland, 7th edn, 2008.
47 A. Karmakar and J. B. Baruah, *Polyhedron*, 2008, **27**, 3409–3416.
48 K. Yadava and J. J. Vittal, *Cryst. Growth Des.*, 2019, **19**, 2542–2547.
49 D. C. Akintayo, W. A. Munzeiwa, S. B. Jonnalagadda and B. Omondi, *Polyhedron*, 2022, **213**, 115589.
50 P. Saxena and N. Thirupathi, *Polyhedron*, 2015, **98**, 238–250.
51 E. A. H. Griffith, N. G. Charles and E. L. Amma, *Acta Crystallogr., Sect. C: Cryst. Struct. Commun.*, 1985, **41**, 673–678.
52 M.-S. Chen, C.-H. Zhang, D.-Z. Kuang, Y.-L. Feng and Y.-F. Deng, *Acta Crystallogr., Sect. E: Struct. Rep. Online*, 2007, **63**, m1290–m1291.
53 Y.-Q. Yang, C.-H. Li, W. Li, D.-C. Guo and Y.-F. Kuang, *Chin. J. Struct. Chem.*, 2006, **25**, 1409–1413.
54 X.-F. Zheng, X.-Q. Shen, X.-S. Wan, H.-Y. Zhang, H. Wang, R. Yang and C.-Y. Niu, *J. Coord. Chem.*, 2007, **60**, 1317–1325.
55 R. Brahma and J. B. Baruah, *ACS Omega*, 2020, **5**, 3774–3785.
56 C. B. Aakeröy, B. M. T. Scott, M. M. Smith, J. F. Urbina and J. Desper, *Inorg. Chem.*, 2009, **48**, 4052–4061.
57 P. Li, D. Zhang, Y. Zhang, W. Lu, J. Zhang, W. Wang, Q. He, P. Théato and T. Chen, *ACS Macro Lett.*, 2019, **8**, 937–942.
58 R. F. Chen, *Anal. Lett.*, 1967, **1**, 35–42.
59 G. M. Hale and M. R. Querry, *Appl. Opt.*, 1973, **12**, 555–563.
60 H. El-Kashef, *Phys. B*, 2000, **279**, 295–301.
61 K. Moutzouris, M. Papamichael, S. C. Betsis, I. Stavrakas, G. Hloupis and D. Triantis, *Appl. Phys. B: Lasers Opt.*, 2014, **116**, 617–622.
62 P. L. Muiño and P. R. Callis, *J. Phys. Chem. B*, 2009, **113**, 2572–2577.
63 A. Kobayashi, R. Arata, T. Ogawa, M. Yoshida and M. Kato, *Inorg. Chem.*, 2017, **56**, 4280–4288.
64 F. W. Steuber, J. J. Gough, É. Whelan, L. Burtnyak, A. L. Bradley and W. Schmitt, *Inorg. Chem.*, 2020, **59**, 17244–17250.
65 D. Ejarque, F. Sánchez-Férez, T. Calvet, M. Font-Bardia and J. Pons, *Inorg. Chim. Acta*, 2020, **509**, 119695.
66 D. L. Kepert, *Inorganic Stereochemistry*, Springer, Berlin, Heidelberg, 1982, vol. 6.
67 R. Hoffmann, B. F. Beier, E. L. Muetterties and A. R. Rossi, *Inorg. Chem.*, 1977, **16**, 511–522.
68 Z. Lin and I. Bytheway, *Inorg. Chem.*, 1996, **35**, 594–603.
69 D. Casanova, P. Alemany, J. M. Bofill and S. Alvarez, *Chem. – Eur. J.*, 2003, **9**, 1281–1295.
70 M. K. Sharma and P. K. Bharadwaj, *Inorg. Chem.*, 2011, **50**, 1889–1897.
71 M. A. Shmelev, G. N. Kuznetsova, N. V. Gogoleva, F. M. Dolgushin, M. A. Kiskin, A. A. Sidorov and I. L. Eremenko, *Russ. Chem. Bull.*, 2021, **70**, 830–838.
72 B. Notash, M. Farhadi Rodbari, G. Gallo and R. Dinnebier, *Inorg. Chem.*, 2021, **60**, 9212–9223.
73 Q.-Q. Li, H. Liu, T.-T. Zheng, P. Liu, J.-X. Song and Y.-Y. Wang, *CrystEngComm*, 2020, **22**, 6750–6775.

 This journal is © The Royal Society of Chemistry 2023